atoms

MDPI

Article

The XSTAR Atomic Database

Claudio Mendoza [1,2,*], Manuel A. Bautista [1], Jérôme Deprince [3], Javier A. García [4,5], Efraín Gatuzz [6], Thomas W. Gorczyca [1], Timothy R. Kallman [7], Patrick Palmeri [3], Pascal Quinet [3,8] and Michael C. Witthoeft [7,9]

1 Department of Physics, Western Michigan University, Kalamazoo, MI 49008, USA; manuel.bautista@wmich.edu (M.A.B.); thomas.gorczyca@wmich.edu (T.W.G.)
2 Physics Center, Venezuelan Institute for Scientific Research (IVIC), Caracas 1020, Venezuela
3 Physique Atomique et Astrophysique, Université de Mons—UMONS, B-7000 Mons, Belgium; jerome.deprince@umons.ac.be (J.D.); patrick.palmeri@umons.ac.be (P.P.); pascal.quinet@umons.ac.be (P.Q.)
4 Cahill Center for Astronomy and Astrophysics, California Institute of Technology, Pasadena, CA 91125, USA; javier@caltech.edu
5 Dr. Karl Remeis-Observatory and Erlangen Centre for Astroparticle Physics, Sternwartstr. 7, 96049 Bamberg, Germany
6 Max Planck Institute for Extraterrestrial Physics, Gießenbachstraße 1, 85748 Garching bei München, Germany; efraingatuzz@gmail.com
7 NASA Goddard Space Flight Center, Greenbelt, MD 20771, USA; timothy.r.kallman@nasa.gov (T.R.K.); michael.c.witthoeft@nasa.gov (M.C.W.)
8 IPNAS, Université de Liège, Sart Tilman, B-4000 Liège, Belgium
9 ADNET Systems Inc., Bethesda, MD 20817, USA
* Correspondence: claudio.mendozaguardia@wmich.edu; Tel.: +1-269-387-4935

Abstract: We describe the atomic database of the XSTAR spectral modeling code, summarizing the systematic upgrades carried out in the past twenty years to enable the modeling of K-lines from chemical elements with atomic number $Z \leq 30$ and recent extensions to handle high-density plasmas. Such plasma environments are found, for instance, in the inner region of accretion disks round compact objects (neutron stars and black holes), which emit rich information about the system's physical properties. Our intention is to offer a reliable modeling tool to take advantage of the outstanding spectral capabilities of the new generation of X-ray space telescopes (e.g., XRISM and ATHENA) to be launched in the coming years. Data curatorial aspects are discussed and an updated list of reference sources is compiled to improve the database provenance metadata. Two XSTAR spin-offs—the `ISMabs` absorption model and the `uaDB` database—are also described.

Keywords: XSTAR; atomic databases; atomic processes; line formation; X-rays; high-density plasmas

Citation: Mendoza, C.; Bautista, M.A.; Deprince, J.; García, J.A.; Gatuzz, E.; Gorczyca, T.W.; Kallman, T.R.; Palmeri, P.; Quinet, P.; Witthoeft, M.C. The XSTAR Atomic Database. *Atoms* **2021**, *9*, 12. https://doi.org/10.3390/atoms9010012

Academic Editor: Claudio Mendoza
Received: 3 December 2020
Accepted: 27 January 2021
Published: 5 February 2021

1. Introduction

The XSTAR (https://heasarc.gsfc.nasa.gov/docs/software/xstar/xstar.html) code computes the physical conditions and emission spectra of a photoionized gas and has been widely used in astrophysics, most notably in X-ray astronomy, for the past 20 years [1,2]. It assumes an ionizing radiation source surrounded by a spherical gas shell that absorbs and transfers parts of this radiation to finally emit a spectrum. From an input comprising the incident continuum, shell thickness, elemental abundances, and gas density, the code computes the ionization balance, level populations, and temperature to generate the gas opacity and the emitted line and continuum fluxes. The computational model determines simultaneously the gas state and radiation field at every user-defined spatial zone of the cloud. To ensure convergence in local thermodynamic equilibrium (LTE) conditions, it implements a detailed and consistent treatment of the radiative (bound–bound, bound–free, and free–free) and collisional (electron-impact excitation and ionization, electron–ion recombination, charge transfer and three-body recombination) processes, a procedure that in turn depends on the accuracy of the underlying database of atomic rate coefficients.

Therefore, XSTAR is an ideal platform to study data curation schemes for implementing and maintaining application-based atomic databases.

Since 2001, we have been systematically computing for the XSTAR database the atomic data required to model the K-lines and edges of both cosmically abundant and trace elements [3–46]. These X-ray spectral features are prime candidates to devise diagnostics to determine the plasma conditions and chemical abundances in a wide variety of astronomical entities: interstellar, intergalactic, and intra-cluster media; active galactic nuclei (AGN); X-ray binaries; supernova remnants; stars; the Sun, and some solar planets and satellites. This long-term collaboration has reached an important milestone, and the corresponding upgrading of the XSTAR database with the new datasets has more than doubled its volume, bringing to the fore a series of data curational problems discussed in this report. Our final goal is to upgrade XSTAR to take advantage of the relatively high spectral resolution (5 eV in the soft X-ray band ∼0.3–12 keV) and sensitivity of the microcalorimeter-based spectrometers in the joint NASA/JAXA X-ray Imaging and Spectroscopy Mission (XRISM, https://heasarc.gsfc.nasa.gov/docs/xrism) to be launched in 2022 and in the European Space Agency flagship Advanced Telescope for High-ENergy Astrophysics (ATHENA, https://sci.esa.int/web/athena). As an example of this accuracy level, Figure 1 shows the XSTAR fit in the 6.50–6.60 keV region of the spectrum of the Perseus Cluster taken by the HITOMI (https://www.nasa.gov/hitomi) space telescope before its demise in 2016 [47].

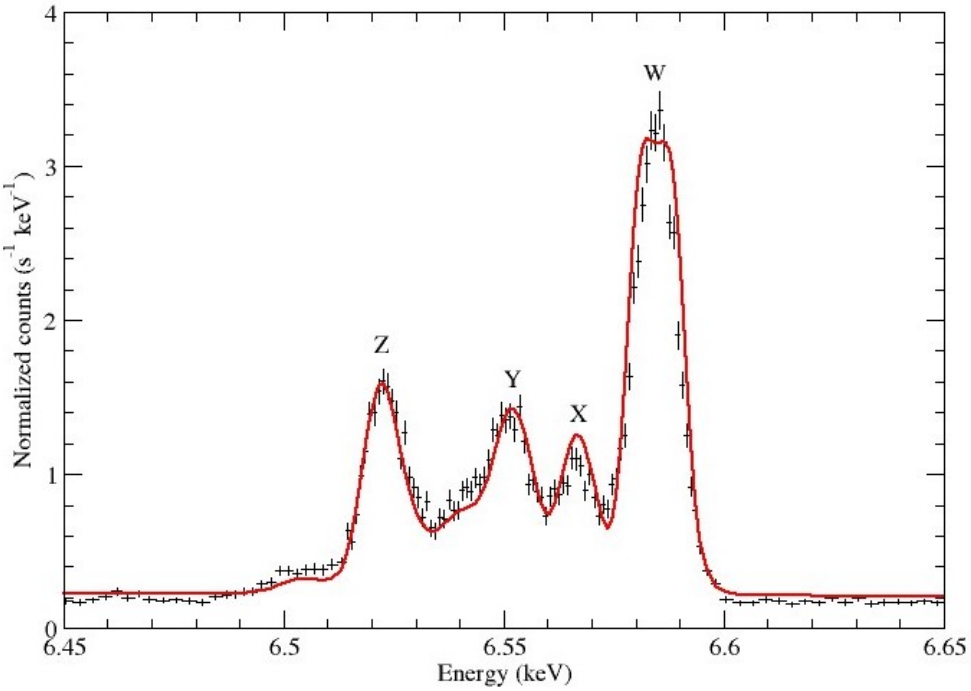

Figure 1. HITOMI spectrum of the Perseus Cluster in the Fe XXV "triplet" spectral region (6.50–6.60 keV) [47] showing the XSTAR fit (red line). With the higher resolution, the He-like "triplet" becomes a quartet comprising the resonance (w), magnetic quadrupole (x), intercombination (y), and magnetic dipole (z) lines. Other Fe satellite lines begin to be detectable (e.g., the bump at ∼6.5 keV).

We have recently introduced high-density ($n_e > 10^{18}$ cm^{-3}) effects in the XSTAR database, which come into play in the reflection spectra of the inner region of the accretion disks around compact objects (e.g., black-hole candidates and neutron stars): continuum lowering [40–45]; dielectronic recombination suppression [48,49]; collisional ionization; three-body recombination; and stimulated emission. Since the Fe abundance is a key measure of line reprocessing in reflection models [50], we are now in a good position to test if the neglect of such high-density effects is responsible for the anomalously high abundances recurrently derived [51]. Regarding XSTAR database curation, the inclusion of

high-density effects presents serious execution difficulties that are now managed by pre-processing the database at each density point. Since this pre-processing time is generally long, a grid of pre-computed databases has been deployed that, considering the data volumes involved, favors a cloud computing environment for the XSTAR modeling of high-density plasmas.

Finally, the development of the XSTAR database has given rise to two spin-offs: the `ISMabs` (https://heasarc.gsfc.nasa.gov/xanadu/xspec/models/ismabs.html) absorption model [35] and the `uaDB` (https://heasarc.gsfc.nasa.gov/uadb/index.php) online database. The former is the result of benchmarks of the theoretical photoionization curves with observed K absorption in the interstellar medium (ISM), which has led to the implementation of a reliable model of ISM K absorption and to the matching of the theoretical K-line wavelengths with the astronomically observed and laboratory measured values, the latter two not always agreeing (e.g., O I [23,52]). The `uaDB` database allows the downloading of the XSTAR and other atomic rates without having to interfere with the code.

2. XSTAR Atomic Database

The XSTAR database comprises records of multilevel model ions (usually referred to as ion targets) and data structures to derive the rates for the microprocesses that determine the ionization and excitation of the plasma [2]. The rate types (*rt*) are the following:

01. Ground state ionization
03. Bound–bound collision
04. Bound–bound radiative
05. Bound–free collision (level)
06. Total recombination
07. Bound–free radiative (level)
08. Total recombination forcing normalization
09. Two-photon decay
11. Element data
12. Ion data
13. Level data
14. Bound–bound radiative, superlevel to spectroscopic level
15. Collisional ionization total rate
40. Bound–bound collisional, superlevel to spectroscopic level
41. Non-radiative Auger transition
42. Inner-shell photoabsorption followed by autoionization.

For each ionic species $(Z; N)$ in the ranges $1 \leq Z \leq 30$ and $1 \leq N \leq Z$, where Z and N are, respectively, the atomic and electron numbers, the data for the target models and processes are contained in ASCII files labeled `d`ion`t0`dt. The ion index ion is defined as

$$ion = Z(Z-1)/2 + (Z-N) + 1\,, \tag{1}$$

and dt is the data type (see Appendix A for a complete list). Each `d`ion`t0`dt file contains integer, floating-point, and character variables. For each release, the database is transcribed to a binary FITS-format-derived [53,54] structure (`atdb.fits`) consisting of three one-dimensional arrays (floating point, integer, and character) and a pointer array, which are uploaded in main memory at runtime. This scheme ensures portability, fast data uploading when the code is invoked, and single-data accesses in main memory during processing.

The XSTAR data curation strategy essentially follows two principles:

1. Since the datasets are compiled from diverse sources, the original data structures and units are explicitly kept in the database records to be transcribed and unified at runtime. For instance, level energies are specified in eV but the photoionization cross-sections are usually tabulated in Rydbergs. Levels in some atomic models are listed in intermediate coupling (fine structure) while in others *LS* terms are adopted.

These format differences are accounted for by defining data types, each of which adheres to its own set of rules for data tabulation.

2. As new data and processes are included in the database, new data types may be defined. Thus, photoionization cross-sections can be specified in more than one data type—valence shell and K shell, say—if the tabulation for each energy region comes from different sources. They are then concatenated and adjusted at runtime.

We show in Figure 2 the target model for Mg-like Zn XIX complying with data type $dt = 06$ and contained in file `d454t006`. Each row is headed by the integer tuple $(dt, rt, 0, N_{\rm flt}, N_{\rm int}, N_{\rm chr})$, where dt is the data type, rt the rate type, $N_{\rm flt}$ the number of floating-point parameters, $N_{\rm int}$ number of integer parameters, and $N_{\rm chr}$ the length of the character string. As shown in the rate-type list above, $rt = 13$ corresponds to level data. The first and second floating-point columns tabulate level energies (eV) and statistical weights $g = 2J + 1$ (the other two floating-point columns have been edited out). The second integer tuple $(n, 2S + 1, L, Z, i, ion)$ lists: the n principal quantum number of the valence electron; the $2S + 1$ spin multiplicity; the total orbital angular momentum L; element atomic number Z; the i level index, and ion index. The character string gives the level assignment (configuration and spectroscopic term), the end of the record being indicated with the % character. Records may span one arbitrary length line or multiple lines in the ASCII file.

```
6 13 0 4 6  8 0.0000000E+00  1.0000000E+00 ...  3 1 0 30  1 454 3s2.1S_0 %
6 13 0 4 6 12 3.6651995E+01  1.0000000E+00 ...  3 3 1 30  2 454 3s1.3p1.3P_0 %
6 13 0 4 6 12 3.8015000E+01  3.0000000E+00 ...  3 3 1 30  3 454 3s1.3p1.3P_1 %
6 13 0 4 6 12 4.1638999E+01  5.0000000E+00 ...  3 3 1 30  4 454 3s1.3p1.3P_2 %
6 13 0 4 6 12 5.6705005E+01  3.0000000E+00 ...  3 1 1 30  5 454 3s1.3p1.1P_1 %
6 13 0 4 6 12 8.8177000E+01  1.0000000E+00 ...  3 3 1 306 454 3s0.3p2.3P_0 %
6 13 0 4 6 12 8.9971999E+01  3.0000000E+00 ...  3 3 1 30  7 454 3s0.3p2.3P_1 %
6 13 0 4 6 12 9.0909009E+01  5.0000000E+00 ...  3 3 1 30  8 454 3s0.3p2.3P_2 %
6 13 0 4 6 12 9.5230001E+01  5.0000000E+00 ...  3 1 2 30  9 454 3s0.3p2.1D_2 %
6 13 0 4 6 12 1.0956001E+02  1.0000000E+00 ...  3 1 0 30 10 454 3s0.3p2.1S_0 %
6 13 0 4 6 16 1.0583000E+03  3.0000000E+00 ...  3 3 0 30 11 454 2p5.3s2.3p1.3S_1 %
6 13 0 4 6 16 1.0607000E+03  5.0000000E+00 ...  3 3 2 30 12 454 2p5.3s2.3p1.3D_2 %
6 13 0 4 6 16 1.0645000E+03  7.0000000E+00 ...  3 3 2 30 13 454 2p5.3s2.3p1.3D_3 %
6 13 0 4 6 16 1.0654000E+03  3.0000000E+00 ...  3 1 1 30 14 454 2p5.3s2.3p1.1P_1 %
6 13 0 4 6 16 1.0674000E+03  5.0000000E+00 ...  3 3 1 30 15 454 2p5.3s2.3p1.3P_2 %
6 13 0 4 6 16 1.0766000E+03  1.0000000E+00 ...  3 3 1 30 16 454 2p5.3s2.3p1.3P_0 %
6 13 0 4 6 16 1.0843000E+03  3.0000000E+00 ...  3 3 2 30 17 454 2p5.3s2.3p1.3D_1 %
6 13 0 4 6 16 1.0895000E+03  3.0000000E+00 ...  3 3 1 30 18 454 2p5.3s2.3p1.3P_1 %
6 13 0 4 6 16 1.0901000E+03  5.0000000E+00 ...  3 1 2 30 19 454 2p5.3s2.3p1.1D_2 %
6 13 0 4 6 16 1.1029000E+03  1.0000000E+00 ...  3 1 0 30 20 454 2p5.3s2.3p1.1S_0 %
6 13 0 4 6 20 1.2384461E+03  1.0000000E+00 ...  3 3 1 30 21 454 2s1.2p6.3s2.3p1.3P_0 %
6 13 0 4 6 20 1.2391314E+03  3.0000000E+00 ...  3 3 1 30 22 454 2s1.2p6.3s2.3p1.3P_1 %
6 13 0 4 6 20 1.2434606E+03  5.0000000E+00 ...  3 3 1 30 23 454 2s1.2p6.3s2.3p1.3P_2 %
6 13 0 4 6 20 1.2457835E+03  3.0000000E+00 ...  3 1 1 30 24 454 2s1.2p6.3s2.3p1.1P_1 %
6 13 0 4 6 24 9.7285003E+03  1.0000000E+00 ...  3 3 1 30 25 454 1s1.2s2.2p6.3s2.3p1.3P_0 %
6 13 0 4 6 24 9.7293003E+03  3.0000000E+00 ...  3 3 1 30 26 454 1s1.2s2.2p6.3s2.3p1.3P_1 %
6 13 0 4 6 24 9.7340004E+03  5.0000000E+00 ...  3 3 1 30 27 454 1s1.2s2.2p6.3s2.3p1.3P_2 %
6 13 0 4 6 24 9.7373003E+03  3.0000000E+00 ...  3 1 1 30 28 454 1s1.2s2.2p6.3s2.3p1.1P_1 %
6 13 0 4 6 10 6.6340128E+02  2.0000000E+00 ... 12 1 0 30 29 454 superlevel %
6 13 0 4 6 14 1.0768748E+04  1.0000000E+00 ...  1 0 0 30 30 454 superlevel_[K] %
6 13 0 4 6  9 6.9751000E+02  2.0000000E+00 ...  3 2 0 30 31 454 continuum %
```

Figure 2. Content of file `d454t006` of the XSTAR database listing the atomic model (data type $dt = 06$ and rate type $rt = 13$) for Mg-like Zn XIX ($ion = 454$).

This ion representation presents remarkable features. By looking at the level-i index and assignment, the Zn XIX model contains data attributes for 31 levels from: the valence shell ($1 \leq i \leq 10$), open L shell ($11 \leq i \leq 24$), and open K shell ($25 \leq i \leq 28$); two superlevels (i = 29–30); and a continuum level ($i = 31$). The latter is associated to the ionization potential of the ion. Therefore, the model comprises spectroscopic bound levels, quasi-bound L- and K-vacancy resonances, and artificial levels. The tabulation must identify the ground level with index 1 and the continuum level with the highest index. Apart from this constraint, the levels are not necessarily listed in energy order facilitating model upgrading, which simply involves adding new levels at the end of the existing

tabulation. The level-assignment string has been carefully devised and used throughout to facilitate searches based on filled shells, shell holes, *LS* terms, and *J* total angular momenta.

Following [1], the `superlevel` accounts in H- and He-like ions for the recombination cascade from unaccounted high-lying levels to the spectroscopic levels of the model atom. Rates have been determined from population kinetic calculations. For other isoelectronic sequences, the `superlevel` is assumed to decay radiatively and collisionally to the ground state. Rates populating and depopulating the `superlevel` are then calculated by fitting to the total recombination rate, thus explicitly accounting for the contributions from excitation, ionization, and recombination to the level populations. As a result, every ionic process is accompanied by its detailed-balance inverse, ensuring the progressive convergence to the LTE level populations. The `superlevel_[K]` is defined in Section 3.1.

All other data types follow similar data structures (floating point, integer, and character) as those displayed in Figure 2. For instance, we show in Figure 3 an excerpt of file `d454t050` containing radiative data for the bound–bound transitions (upper level $k \leq 10$) in Zn XIX. As before, the header integer tuple prescribes the data and rate types $dt = 50$ and $rt = 4$; three floating-point items; four integer items; and no character strings. The floating-point tuple $(\lambda, gf(i,k), A(k,i))$ lists the transition wavelength (Å), oscillator strength (gf-value), and transition probability (A-value, s^{-1}). The second integer tuple (i, k, Z, ion) lists the lower and upper levels of the transition, atomic number, and ion index. By comparing the i and k transition indices with the i level indices in Figure 2, it may be seen that the tabulation includes both allowed and forbidden transitions, e.g., the resonance transition $(i,k) = (1,5)$ and the forbidden transition $(i,k) = (1,4)$. Importantly, every excited level in the database must include a decay mechanism, radiative and/or collisional; otherwise, its population may grow out of bounds when modeling. For instance, the 3s1.3p1.3P_0 metastable level ($i = 2$) does not display a radiative transition ($j = 0 \rightarrow 0$ radiative transitions are strictly forbidden), and consequently, an alternative decay process must be provided in a separate data type; e.g., collisional de-excitation.

```
50 4 0 3 4 0   3.2047230E+02  5.2260000E-03  1.1310000E+08 1  3 30 454  %
50 4 0 3 4 0   2.0629320E+02  7.0930000E-01  3.7060000E+10 1  5 30 454  %
50 4 0 3 4 0   2.4417010E+02  2.5340000E-01  2.8350000E+10 3  6 30 454  %
50 4 0 3 4 0   4.2222080E+02  4.7650000E-03  1.7830000E+08 5  6 30 454  %
50 4 0 3 4 0   2.2582420E+02  2.7330000E-01  1.1910000E+10 2  7 30 454  %
50 4 0 3 4 0   2.3171380E+02  1.9730000E-01  8.1690000E+09 3  7 30 454  %
50 4 0 3 4 0   2.4845700E+02  3.1050000E-01  1.1180000E+10 4  7 30 454  %
50 4 0 3 4 0   3.8631020E+02  1.4800000E-03  2.2060000E+07 5  7 30 454  %
50 4 0 3 4 0   2.2265070E+02  3.4070000E-01  9.1680000E+09 3  8 30 454  %
50 4 0 3 4 0   2.3806620E+02  7.8830000E-01  1.8560000E+10 4  8 30 454  %
50 4 0 3 4 0   3.6175990E+02  1.2440000E-01  1.2680000E+09 5  8 30 454  %
50 4 0 3 4 0   2.0084360E+02  2.0630000E-02  6.8230000E+08 3  9 30 454  %
50 4 0 3 4 0   2.1330280E+02  2.0500000E-01  6.0100000E+09 4  9 30 454  %
50 4 0 3 4 0   3.0751030E+02  8.4760000E-01  1.1960000E+10 5  9 30 454  %
50 4 0 3 4 0   1.7136220E+02  2.6040000E-03  5.9150000E+08 3 10 30 454  %
50 4 0 3 4 0   2.4339670E+02  3.8770000E-01  4.3650000E+10 5 10 30 454  %
50 4 0 3 4 0   2.9315000E+02  0.0000000E+00  9.5940000E+00 1  4 30 454  %
```

Figure 3. Excerpt of file `d454t050` of the XSTAR database listing the radiative transitions with upper level $k \leq 10$ (data type $dt = 50$ and rate type $rt = 4$) in Mg-like Zn XIX ($ion = 454$).

Data type $dt = 86$, listing the radiative and Auger widths of K-vacancy levels, is also an interesting case as it involves transitions between different ion-charge states (Figure 4). The floating-point tuple $(E(k_N), A_a(k_N), A_a(k_N, i_{N-1}), A_r(k_N))$ lists: the energy $E(k_N)$ (in eV relative to the ionization threshold) and total Auger width $A_a(k_N)$ (s^{-1}) of the k_N level of the N-electron ion ($ion_N = 454$); the partial Auger width $A_a(k_N, i_{N-1})$ (s^{-1}) leaving the $(N-1)$-electron ion ($ion_{N-1} = 455$) in the i_{N-1} level; and the total radiative width $A_r(k_N)$ (s^{-1}) of the k_N level of the N-electron ion. The second integer tuple then specifies $(i_{N-1}, k_N, Z, ion_{N-1}, ion_N)$. In this example, the $(N-1)$-electron ion is assumed to end up in its ground state ($i_{N-1} = 1$) after the Auger transition; however, this is not always

the case as the Auger transition may involve an excited end level of the $(N-1)$-electron ion. Such partial Auger widths are not determined in some structure codes (e.g., HFR [55]) and in the *R*-matrix scattering method [56,57], the latter including radiative and Auger damping through an optical model potential [58].

```
86 4 0 4 5 0   9.0309903E+03  1.1100000E+15  1.1100000E+15  1.1600000E+15 1 25 30 455 454 %
86 4 0 4 5 0   9.0317903E+03  1.1000000E+15  1.1000000E+15  1.1800000E+15 1 26 30 455 454 %
86 4 0 4 5 0   9.0364904E+03  1.1000000E+15  1.1000000E+15  1.1600000E+15 1 27 30 455 454 %
86 4 0 4 5 0   9.0397903E+03  1.0800000E+15  1.0800000E+15  1.2900000E+15 1 28 30 455 454 %
```

Figure 4. Content of file d454t086 of the XSTAR database listing the radiative and Auger widths (data type $dt = 86$ and rate type $rt = 4$) of Mg-like Zn XIX ($ion = 454$).

Table A1 in Appendix B tabulates the number of levels for each ionic species $(Z; N)$. It may be seen that most neutral and, in many cases, the singly ionized systems are not well represented, indicating that XSTAR is mainly destined to model photoionized plasmas for which such species have negligible fractions. The number of levels in the ion models is never above 1000 to enable practical runtimes when modeling (see Section 6.1), and the most relevant elements in the astronomical soft X-ray band—N, O, Ne, Fe, and Ni—are especially well treated.

As fully described in the original paper on the XSTAR database [2], atomic datasets have been collected from a myriad of individual sources and data compilations such as the NIST Atomic Spectra Database (https://www.nist.gov/pml/atomic-spectra-database) [59], TOPbase (http://cdsweb.u-strasbg.fr/topbase/topbase.html) [60], CHIANTI (https://www.chiantidatabase.org/) [61], ADAS (https://www.adas.ac.uk/), Iron Project (http://cdsweb.u-strasbg.fr/topbase/testop/TheIP.html) [62], and PP95 (https://ned.ipac.caltech.edu/level5/Pradhan/Pradhan_contents.html) [63]. Major upgrades have been mainly concerned with the radiative recombination (RR) and dielectronic recombination (DR) data from the AMDPP tabulations (http://amdpp.phys.strath.ac.uk/tamoc/DATA/) [64,65] and from the systematic computations of atomic data for K-line diagnostics summarized in the next Section 3. A complete data provenance list is given in Appendix C.

3. Computation of Atomic Data for K-Line Diagnostics

Since XSTAR is widely used for spectral modeling in X-ray astrophysics, we have dedicated a systematic effort to compute the atomic data to characterize K-lines in ionic species with $Z \leq 30$—namely, valence and K-vacancy level energies, transition wavelengths, *A*-values, radiative and Auger widths, and photoionization cross-sections [5–29]. Due to the lack of spectroscopic data to validate most ionic models, a multi-code methodology was implemented right from the outset to compute the data and estimate their accuracy. Structure data were computed with the multiconfiguration codes HFR (Pauli Hamiltonian) [55], AUTOSTRUCTURE (Breit–Pauli Hamiltonian) [66,67], and GRASP92 (Dirac–Coulomb–Breit Hamiltonian) [68], and the photoionization cross-sections with the Breit–Pauli *R*-matrix suite of codes [56,57] and AUTOSTRUCTURE. Due to the large target models for species in isoelectronic sequences with electron number $19 \leq N \leq 26$, the latter code was used to compute their photoionization cross-sections in the distorted-wave approximation. Initial priority was given to ions from the oxygen, nitrogen, and iron isonuclear sequences and then from even-*Z* elements, but those from odd-*Z* and trace elements have been recently completed.

In the calculations of accurate atomic data for K-line diagnostics, two key effects must be considered in detail: radiative and Auger damping and orbital relaxation. In Sections 3.1 and 3.2, we briefly outline these two processes and the methods to include them in structure and scattering calculations.

3.1. Radiative and Auger Damping

Let us consider an ion, say, with electron number $N \leq 10$. When a photon promotes a K-shell electron to an excited Rydberg state,

$$h\nu + 1s^2 2s^\lambda 2p^\mu \longrightarrow 1s2s^\lambda 2p^\mu np\,, \tag{2}$$

it subsequently decays via the radiative and Auger manifold

$$1s2s^\lambda 2p^\mu np \xrightarrow{Kn} 1s^2 2s^\lambda 2p^\mu + h\nu_n \tag{3}$$

$$\xrightarrow{K\alpha} 1s^2 2s^\lambda 2p^{\mu-1} np + h\nu_\alpha \tag{4}$$

$$\xrightarrow{KLn} \begin{cases} 1s^2 2s^\lambda 2p^{\mu-1} + e^- \\ 1s^2 2s^{\lambda-1} 2p^\mu + e^- \end{cases} \tag{5}$$

$$\xrightarrow{KLL} \begin{cases} 1s^2 2s^\lambda 2p^{\mu-2} np + e^- \\ 1s^2 2s^{\lambda-1} 2p^{\mu-1} np + e^- \\ 1s^2 2p^{\mu-2} np + e^- \end{cases} \tag{6}$$

dominated by Kα radiative decay (Equation (4)) and KLL Auger spectator-electron ionization (Equation (6)). Such channeling causes a damping effect (see Figure 5) since the $1s2s^\lambda 2p^\mu np$ resonances have broad and symmetric widths almost independent of n, which must be taken into account when devising plasma diagnostics. In the R-matrix method, it is computationally intractable to treat this channel array from first principles as it would involve target states with np orbitals in an ever increasing close-coupling expansion. Therefore, for the higher Rydberg resonances, damping is neatly accounted for via an additional imaginary potential $V_{\rm opt} = -i(\Gamma_r + \Gamma_a)/2$ involving the total radiative width Γ_r—as developed in the Hickman–Robicheaux formalism [69,70] (which is essentially equivalent to the Davies–Seaton formalism [71,72])—and adapted to include the total Auger width Γ_a [58].

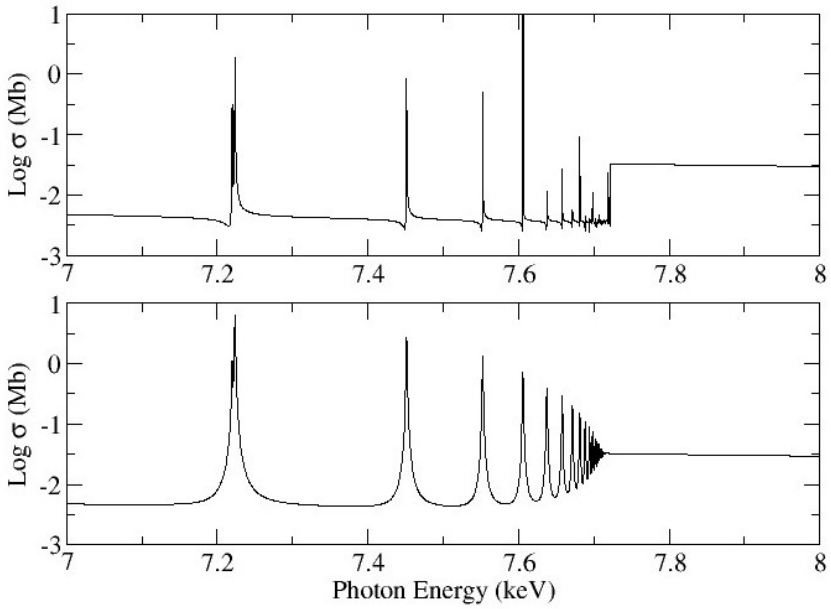

Figure 5. Photoabsorption cross-section of the $1s^2 2s^2 2p^6\ ^1S$ ground state of Ne-like Fe XVII in the K-edge region. *Top panel*: undamped cross-section. *Bottom panel*: damped (radiation and Auger) cross-section.

Due to their diagnostic importance, Kα lines in the XSTAR database are treated as bound–bound transitions and assigned wavelengths and A-values, but the upper K-vacancy states also display Auger widths that lead to autoionization (see Figures 2–4). However, the K resonances also appear in the photoabsorption cross-sections, as shown in

Figure 5, smearing the edge due to their peculiarly symmetric and constant line profiles. As a result, the Kα resonances must be trimmed out from the partial photoionization cross-sections that are used to derive the rates so as not to count them twice. However, it is more complicated to carry out this trimming procedure in the L-edge region due to the piling up of a large number of resonances converging to closely spaced thresholds; thus some degree of double counting is practically unavoidable, making the L-edge less useful to devise plasma diagnostics.

As shown in Figure 6, damping leads to a significant difference between photoabsorption and photoionization, and in the XSTAR code, both are needed: the former to determine opacities and the latter to derive the photoionization rates. However, the database essentially stores partial photoionization cross-sections, i.e., cross-sections leaving the photoionized $(N-1)$-electron system in specific states, and consequently, the difference between the total photoabsorption and photoionization cross-sections is assigned to `superlevel_[K]` (see level $i = 30$ in Figure 2).

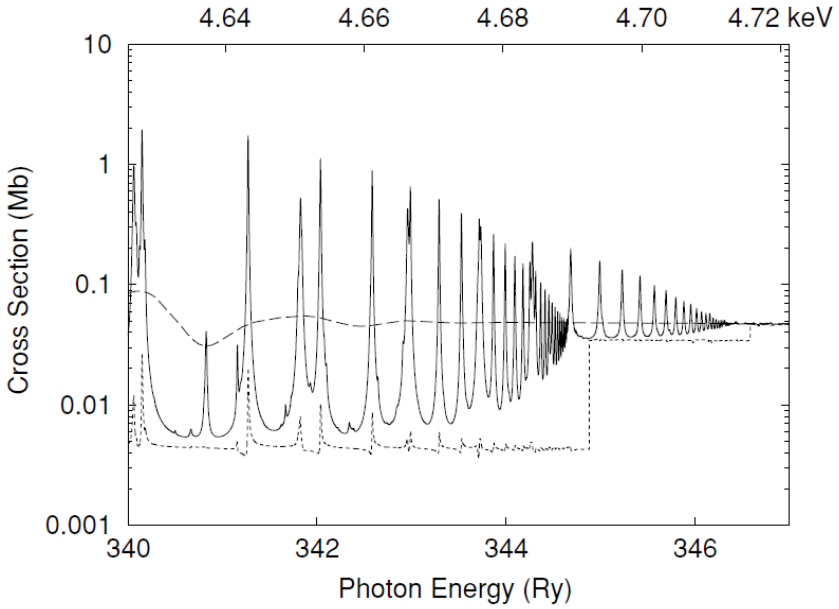

Figure 6. K-edge photoabsorption (full curve) and photoionization (dotted curve) cross-sections of Ca XV (C-like) as a function of photon energy. The dashed curve gives the photoabsorption cross-section convolved with a Gaussian of 0.001 width. Reproduced from Figure 3 of [18] with permission of the AAS.

Due to the large number of target levels in ions with electron number $N > 18$, their photoionization cross-sections were computed using the simpler distorted-wave method implemented in AUTOSTRUCTURE [29]. The level numbers for such ionic systems tabulated in Table A1 (Appendix B) underwent considerable trimming to comply with the modeling specifications of XSTAR and, hence, do not represent the extent of the actual collisional targets. In AUTOSTRUCTURE, photoabsorption is conveniently treated as the sum of two separate processes: photoionization and photoexcitation. However, the complicated decay routes of K-vacancy states delineated in Equations (3)–(6) must be explicitly included in the photoexcitation process, and were thus computed in *LS* coupling. Since XSTAR requires fine-structure partial photoionization cross-sections to determine rates, we decided to obviate the phototexcitation process in ions with $Z \neq 26$ and $21 \leq N \leq 26$, thus underestimating their opacities, although the radiative and Auger decays of the Lα, β and Kα, β lines from these systems will be respectively taken into account in data types 50 and 86 (see Figures 3 and 4).

3.2. Orbital Relaxation

As shown in [55,73], the photoionization of an inner-shell electron leads to a *relaxation* of the outer electrons of the ionized state due to a reduced screening of the atomic nuclear potential by the reduced inner electron cloud; i.e., an increased effective charge $Z_{\rm eff}$. For example, in the inner-shell photoionization of O I $1s^2 2s^2 2p^4$ to O II $1s 2s^2 2p^4$, the effective charge experienced by a 2p electron in the initial and final states is a complicated average screening including the other equivalent 2p electrons. Nevertheless, by using hydrogenic considerations, it is found that the electron orbital energy ($E_n \sim -E_R\, Z_{\rm eff}^2/n^2$) is more tightly bound for the relaxed 2p electron, and the electron density is concentrated closer to the nucleus ($r_n \sim a_0\, n^2/Z_{\rm eff}$).

To illustrate this phenomenon, we show in Figure 7 the outer 2p orbital in both neutral oxygen and its K-vacancy ionized daughter obtained from single-configuration Hartree–Fock calculations [74,75]. Clearly, the *relaxed* 2p orbital of the ionized O II inner-shell state differs significantly from the neutral O I 2p orbital, a difference that needs to be accounted for to compute more accurate atomic transition properties.

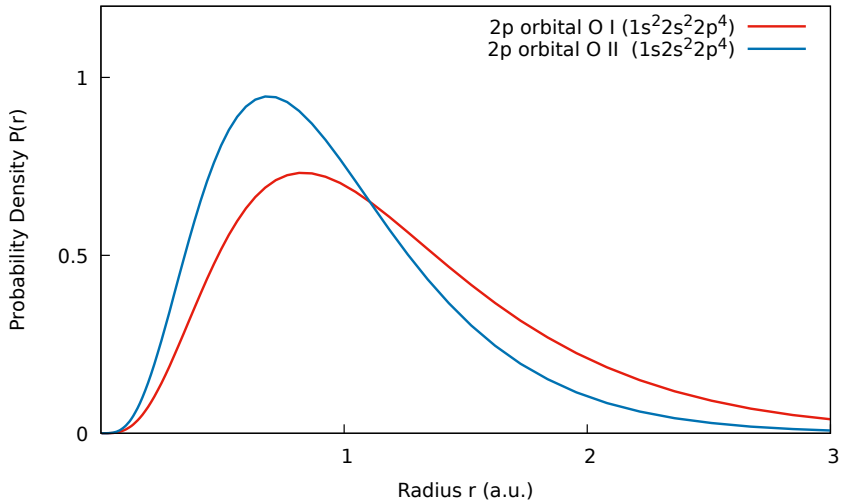

Figure 7. Probability density of the Hartree–Fock 2p orbital in the initial O I $1s^2 2s^2 2p^4$ ground state compared to the 2p orbital in the final O II $1s 2s^2 2p^4$ K-vacancy state. The 2p electrons of the latter are screened from the nucleus by one fewer inner-shell 1s electron and are therefore "relaxed" to more tightly bound orbitals.

In our HFR and AUTOSTRUCTURE structure calculations, orbital relaxation was taken into account by adopting different non-orthogonal orbital bases for each configuration. In most photoionization calculations, however, an orthonormal orbital basis is used because of the relative simplicity in computing transition and energy matrix elements. Relaxation then requires a substantial multi-configurational wave-function description including additional orbitals to account for the significant differences between initial- and final-state orbitals. Thus, additional care must be taken in computing inner-shell photoionization cross-sections when compared to outer-shell photoionization, as discussed more fully in [23]. Due to these difficulties, most large-scale computations of photoabsorption and photoionization cross-sections do not include orbital relaxation effects unless otherwise indicated.

4. Photoabsorption Cross-Section Benchmarks

Table A2 in Appendix C lists the reference sources for the computations of the photoabsorption cross-sections. Measurement of K absorption in the laboratory and ISM enables useful benchmarks of the theoretical cross-sections to improve spectral accuracy. In the following sections, we give a summary of these procedures.

4.1. Carbon Sequence

Calculations of the atomic data to model the K-shell photoabsorption by carbon ions were performed by [21], and a benchmark was obtained using *Chandra* X-ray high-resolution spectra [37]. The C II Kα "triplet" as well as the C III Kα and Kβ lines were identified in the X-ray spectra of four super-soft sources. C I was not modeled due to the presence of instrumental features at ∼43.6 Å.

4.2. Oxygen Sequence

K-shell photoabsorption cross-sections for O I–O VII were computed by [11], and comparisons of the theoretical resonance positions with astronomical observations and laboratory measurements were carried out by [32,33]. It was found that, due to a suspect experimental energy calibration scale, the X-ray astronomical observations provided a more reliable reference to perform the benchmark of the atomic data. For O I, the K-edge cross-section was re-examined in detail to yield a substantially improved version for the XSTAR atomic database [23].

In this exhaustive study, the Kα ($1s \rightarrow 2p$) resonance in O I was examined with *R*-matrix and Multi-Configuration Hartree–Fock (MCHF) calculations, existing laboratory spectroscopic data, and several X-ray observational assessments (see Table 1). While practical *R*-matrix calculations for multi-electron systems are better tailored for computing scattering and atomic transition rates, they are less reliable in predicting the energy differences between atomic states as compared to limited bound-state structure calculations. (*R*-matrix calculations necessarily include all quasi-bound and continuum final states, limiting a practical improvement of the basis description.) The *R*-matrix Kα energy was found to be ∼0.3 eV higher than the final assessed observational value of 527.37 eV [23]. More complex MCHF calculations, which were focused only on the initial $1s^2 2s^2 2p^4$ state and final $1s2s^2 2p^5$ state, converged downward to a value of 527.49 eV, in good agreement with the observations. On the other hand, the experiments performed at the Advanced Light Source (ALS) were reporting a value of 526.79 eV [76], a discrepancy of almost −0.6 eV. Considering the reliability of the observational calibration and the convergence trend of the MCHF calculations, the X-ray observation was unconventionally chosen instead of the laboratory measurement as the final resonance position in the atomic absorption model.

Table 1. Comparison of astronomically observed, laboratory measured, and computed O I Kα and Kβ line energies (eV).

Method	Source	$E(1s-2p)$	$E(1s-3p)$	ΔE
Astronomical observations	*XMM-Newton*, Mrk 421 [23]	527.30(5)	541.95(28)	14.65(33)
	Chandra, 7 sources [23]	527.44(9)	541.72(18)	14.28(21)
	Chandra, shifted [23]	527.26(9)		
	Chandra, 11 sources [77]	527.39(2)		
	Chandra, 6 sources [78]	527.41(18)	541.77(40)	14.36(58)
Laboratory measurements	HZB [52]	527.26(4)	541.645(12)	
	ALS [79,80]	526.79(4)	541.19(4)	14.40(8)
	ALS [76]	526.79(4)	541.20(4)	14.41(8)
	WSRC [81]	527.85(10)	541.27(15)	13.41(25)
	Auger spectroscopy [82]	527.20(30)		
MCHF converged result	MCHF [23]	527.49		

A further consideration in assessing the reliability of the ALS measurements was that the absolute energy calibration relied on earlier molecular measurements with uncertainty estimates that seemed questionable. Since the O I study by [23], new laboratory measurements have been performed using an electron beam ion trap (EBIT) to determine the Kα resonance position at 527.26 ± 0.04 eV [52], in good agreement with the observations and the converged MCHF result. This new measurement suggests a recalibration of the ALS reference spectrum.

4.3. Neon

For neon, the XSTAR atomic database includes the photoabsorption cross-sections by [13]. A benchmark for Ne II and Ne III was performed with *Chandra* and *XMM-Newton* observations of the bright low-mass X-ray binaries (LMXBs) Cygnus X–2 and XTE J1817-330 [35]. Column densities were obtained for the cold (Ne I) and warm (Ne II, Ne III) components of the ISM.

4.4. Magnesium

New photabsorption cross-sections for Mg species were computed by [25]. X-ray *XMM-Newton* spectra of the LMXB GS 1826-238 were used to perform a benchmark of the data. The resulting ionization fractions indicate that Mg is predominantly ionized rather than in neutral form, as also shown by UV observations.

4.5. Silicon

High-resolution *Chandra* spectra in the Si K-edge region (6–7 Å) from 16 LMXBs were analyzed by [39]. The Si model included the Si I photoabsorption cross-sections computed by Gorczyca et al. (2020, in preparation), while those for the ionized species were taken from [18]. The absorption features identified in the spectra agreed with the theoretical atomic data, even though the individual resonances of the Kα "triplet" could not be resolved. Although a model without the dust component was used, good data fits were obtained, highlighting the need for accurate modeling of the gaseous component before attempting to address the solid component [39].

5. High-Density Effects on Atomic Parameters

XSTAR needs to address spectra from high-density sources such as the X-ray reflection from the inner region of the accretion disks around compact objects (electron temperature $T_e \sim 10^5$–10^7 K and density $n_e \sim 10^{18}$–10^{22} cm^{-3}) [51,83]. This requires taking into account a series of atomic processes usually neglected in plasma photoionization models, which have been fully discussed by [46] and recently implemented in the code. We discuss in Sections 5.1 and 5.2 two of these processes—continuum lowering and DR suppression—since they led to significant modifications of the database design and implementation.

5.1. Continuum Lowering

The density effects on the atomic thresholds (ionization potential and K edge), Kα wavelengths and A-values, and Auger rates of oxygen and iron ions have been studied by [40–45]. The atom is assumed to be embedded in a weakly coupled plasma represented in the Multi-Configuration Dirac–Fock (MCDF) method with a time-independent Debye–Hückel screened Dirac–Coulomb Hamiltonian:

$$H_{DC}^{DH} = \sum_i c\vec{\alpha}_i \cdot \vec{p}_i + \beta_i c^2 - \frac{Z}{r_i} e^{-\mu r_i} + \sum_{i>j} \frac{1}{r_{ij}} e^{-\mu r_{ij}} \,, \tag{7}$$

where $r_{ij} = |\vec{r}_i - \vec{r}_j|$ and the plasma screening parameter μ (inverse of the Debye shielding length λ_D) is given in atomic units (λ_D in Bohr radius a_0; n_e in a_0^{-3}; and kT_e in Hartree) by

$$\mu = \frac{1}{\lambda_D} = \sqrt{\frac{4\pi n_e}{kT_e}} \,. \tag{8}$$

As shown in Figure 8, the density effects mainly cause a threshold lowering that increases with μ, which for the ionization potential can be approximated in eV by the universal formula [45] in terms of the effective charge $Z_{\rm eff} = Z - N + 1$

$$\Delta E_0 = (-26.30 \pm 0.08)\mu Z_{\rm eff} \,. \tag{9}$$

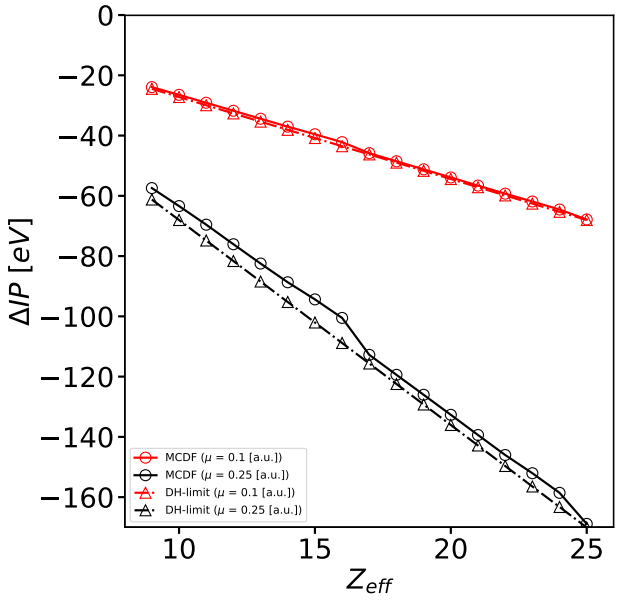

Figure 8. Ionization potential lowering in Fe IX–Fe XXV as a function of effective charge $Z_{\rm eff} = Z - N + 1$ obtained with the MCDF method using a Debye–Hückel screening potential. Red circles: $\mu = 0.1$ a.u. Black circles: $\mu = 0.25$ a.u. Triangles: Debye–Hückel limit $\Delta E_0^{\rm DH} = -27.2116\,\mu Z_{\rm eff}$ eV. Reproduced from Figure 1 of [43] with permission from Astronomy & Astrophysics, ©ESO.

In XSTAR continuum lowering leads to density-dependent targets with reduced numbers of levels, which must be derived at each density point causing a severe overhead at runtime. This bottleneck can be mitigated by pre-computing a μ grid of atomic databases but at the price of increasing the database volume significantly (∼10 GB), thus hampering the standard package downloading procedure. Consequently, deployment strategies are being considered in terms of cloud virtual machines and containers.

5.2. DR Suppression

Rigorous collisional–radiative plasma modeling shows that DR is suppressed at high densities [84]. As mentioned in Section 2, RR and DR rates are treated separately in the XSTAR database using the AMDPP tabulation [64,65], which allows an estimate of the DR-rate density attenuation using the analytic formulae by [48,49]. The highly approximate value of the DR suppression factors has nevertheless been stressed by [49], as well as the need for detailed collisional–radiative calculations. The intermediate density range ($10 \leq \log n_e \leq 18$ cm^{-3}) is expected to be the most susceptible since, at the higher densities ($\log n_e > 18$ cm^{-3}), DR is practically negligible.

It is worth mentioning that in the unified treatment of electron–ion recombination [85,86], where the total recombination rate is obtained directly from a Maxwellian average of the photoionization cross-section through the Milne relation, it would be more difficult to evaluate the DR density effects. It would imply a rigorous approach to introduce plasma interactions in the Hamiltonian, such as those described for continuum lowering (see Section 5.1), followed by large-scale computations of photoionization cross-sections and fitting procedures to obtain a set of interpolation formulae.

To characterize the plasma effects caused by DR suppression, we have compared the heating and cooling rates in the ionization-parameter–temperature plane:

$$-3 \leq \log(\xi) \leq 3 \text{ erg cm s}^{-1} \quad \text{and} \quad 3.5 \leq \log(T) \leq 7.5 \text{ K} \tag{10}$$

for XSTAR models with and without metal DR. We assume a power-law spectrum, density $n_e = 10^{10}$ cm^{-3}, and luminosity $L = 10^{32}$ erg s^{-1} (see Figure 9). The larger temperature differences occur in the interval $1 \leq \log(\xi) \leq 3$, where T is lower by as much as 40% when DR is excluded, and are caused by increases in the Fe average charge at $\log(\xi) \approx 1.3$ and

$\log(\xi) \approx 2.5$. As shown in Figure 9 (right panel), the DR/noDR heating-rate ratio reaches a maximum at $(\log(\xi), \log(T)) \approx (1, 6.3)$, where the dominant species with and without DR are Fe XIII and Fe XVII, respectively. On the other hand, the cooling-rate ratio reaches a maximum at $(\log(\xi), \log(T)) \approx (-1, 5.4)$, caused by a higher oxygen average charge when DR is excluded.

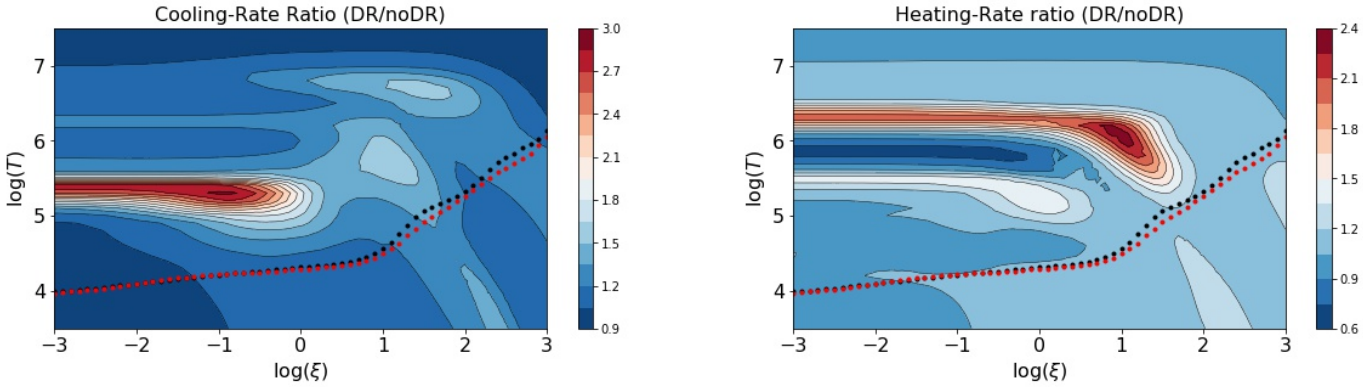

Figure 9. Cooling- and heating-rate ratios with and without DR obtained from an XSTAR model with solar abundances, a power-law spectrum, density $n_e = 10^{10}$ cm^{-3}, and luminosity $L = 10^{32}$ erg s^{-1}. Black dotted curve: thermal temperature with DR. Red dotted curve: thermal temperature without DR.

Concerning the Fe anomalous overabundance derived from the reflection spectra of accretion disks [51], we have computed the X-ray spectra reflected from an optically thick atmosphere using the XILLVER code [87,88]. The atmosphere is assumed to have plane-parallel geometry and a constant gas density of $\log(n_e) = 18$ cm^{-3}. The ionization parameter is set to $\xi = 4\pi F_x/n_e = 32$ erg cm s^{-1} implying an illuminating flux of $F_x = 3 \times 10^{18}$ erg cm^{-2} s^{-1}. The ionization balance is calculated self-consistently using the routines and atomic data from XSTAR, setting all elemental abundances to their solar values. It is found that metal DR suppression leads to significant changes in the ionization state of the gas resulting in more ionized species. As shown in Figure 10, there is a strong enhancement of the Fe XVII L lines and Fe XVIII K lines.

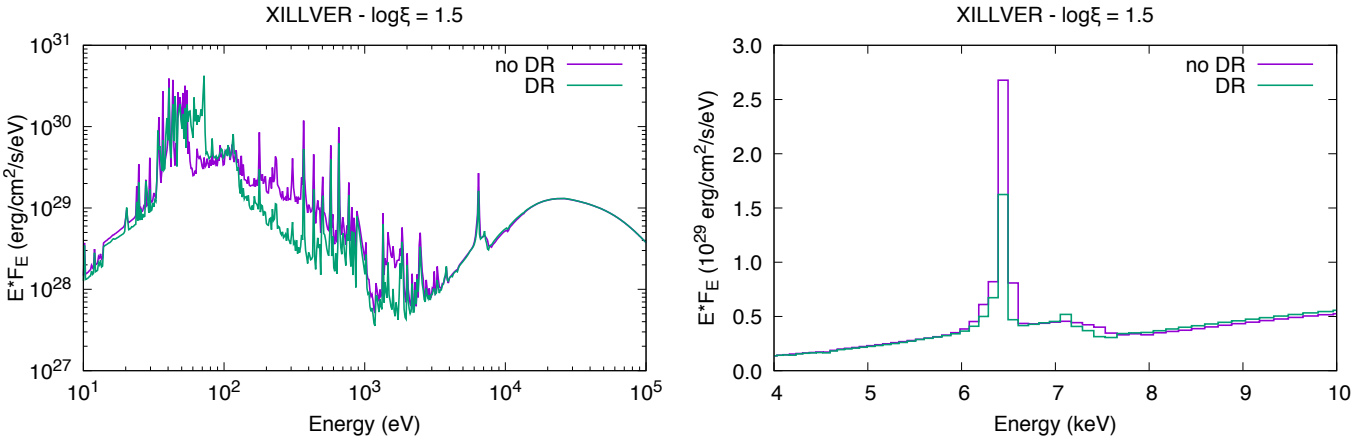

Figure 10. Reflected X-ray spectrum from an optically thick atmosphere modeled using XILLVER with and without DR. A plane-parallel atmosphere with solar abundances and density $\log(n_e) = 18$ cm^{-3} was assumed.

It is worth mentioning that continuum lowering is not taken into account in this XILLVER test calculation since it is expected to have a noticeable impact only at densities $n_e > 10^{19}$ cm^{-3}. The calculation was performed at $n_e = 10^{18}$ cm^{-3} to show that DR effects become conspicuous at lower densities. Further characterization of high-density effects are reported in [46].

Density effects on DR and the high-n levels through continuum lowering are taken into account in the XSTAR database via the rates into one or two superlevels for each ion. The recombination rate onto the superlevel is tabulated on a density–temperature grid and stored in data types 70 and 99 (see Appendix A). For the former, rates are tabulated on a log scale, while for the latter, they are tabulated directly. The total recombination rate onto the ion is the sum of the rate onto the superlevels plus the rates onto the other levels that are treated explicitly; these are called the "spectroscopic levels". The recombination rates onto the superlevels are chosen such that, when they are used to calculate a recombination rate and all the rates are summed up, the total recombination rate for the superlevel(s) plus the spectroscopic levels is equal to the total rate taken from one of the AMDPP compilations [64] where available or from [89] otherwise. We apply density-dependent suppression factors to the recombination rates onto the superlevel to take into account density effects on radiative and dielectronic recombination. They are derived from a general formula that depends on the isoelectronic sequence, charge, density, and temperature [48,49].

The superlevels decay directly to the ground level without the emission of any observable cascade radiation for ions with three or more electrons. The exception is the decay of members of the H and He isoelectronic sequences, for which we use explicitly calculated cascade matrix calculations to treat the decay of the superlevels to the spectroscopic levels [90,91]. The superlevels are chosen to have energies close to the continuum. We include both radiative and collisional transitions to the ground level (and other levels in the case of H- and He-like ions).

6. Database Curation

The recent inclusion in the XSTAR database of atomic parameters for odd-Z elements, $Z = (9, 11, 15, 17, 19)$, and trace elements with $Z = (21\text{–}25, 27, 29, 30)$ [26–29] practically doubled the database volume when compared with previous versions that used hydrogenic scaling for these elements, bringing to the fore a series of curatorial problems. The database upgrade was thus lengthy and demanding in detail. In Sections 6.1–6.4, we give a brief account of some the issues encountered and steps taken to solve them.

6.1. Atomic Models

As shown in Table 9 of [26], the target models for ions with atomic numbers $Z = (21\text{–}25, 27, 29, 30)$ and electron number $19 \leq N \leq Z - 2$ include levels from the valence configurations $\mu = 3d^x 4s^y$ and the L- and K-vacancy configurations $3p^{-1}\mu^{+1}$, $2p^{-1}\mu^{+1}$, and $1s^{-1}\mu^{+1}$. The total number of target levels in each of these species is larger than 500 and in some cases (e.g., $N = 23$) close to 2000. It was found that to model astrophysical plasmas in XSTAR with such large atomic representations was impractical and with little tangible gains. We thus excluded the levels belonging to μ configurations containing 4s orbitals—specifically, $y = 0$ in μ for $N > 19$. This decision led to a reduction in the number of target levels to a few hundreds and implied extensive level renumbering for these sequences.

6.2. Metastable Levels

As discussed in Section 2, the XSTAR atomic models display occasional low-lying metastable levels (e.g., the 3s1.3p1.3P_0 level in Mg-like ions) with no radiative decay transitions. Since metastable lavels in low valence-shell configurations are astrophysically important, alternative decay mechanisms such as collisional de-excitation must be specified for such levels. For instance, we computed a large number of distorted-wave collision strengths with AUTOSTRUCTURE for transitions within the valence-shell configurations of trace-element ions (see record with ID = mb01 and code = 1150 in Table A2). However, for ions with electron number $N > 19$ and ground configuration $3d^x$, atomic models with a few hundred levels must be considered (see Section 6.1), which leads to the appearance of unexpected metastable levels in the $3p^{-1}$ configuration at fairly high energies. Most of these levels were detected by running the code to look for levels with anomalously large populations, which were then removed by hand followed by level reordering.

6.3. Database Pointers

As previously mentioned, the raw XSTAR database consists of a list of ASCII files labeled d*ion*t0*dt*, where *ion* is the ion identifier and *dt* the data type. When the package is released, these files are read into three one-dimensional arrays (integer, real, and character variables) and a set of pointers to be finally structured into the FITS file `atdb.fits`. At runtime, these arrays are read into main memory to be accessed according to the user model. This data structure arrangement is efficient when uploading from disk and during processing, but can be cumbersome in database updating when new record types are created. Proficient nursing and testing are required before the new version is released.

6.4. Metadata

The XSTAR database compiles atomic data computed to order and from a myriad of other data sources. The data provenance of the first release was detailed in [2], but since then, the database has undergone several major upgrades that have not been formally registered within its file structure. One of the aims of the present paper is to create an up-to-date data provenance blueprint to be included in the database using the FITS metadata facilities.

In Table A2 of Appendix C, we have tabulated an up-to-date list of data source references including the original four- and five-letter mnemonics used for identification in [2] and a new four-integer code to be inserted in every database record. For this purpose, we will adopt the third integer (currently displaying a zero) of the record header $(dt, rt, 0, N_{\rm flt}, N_{\rm int}, N_{\rm chr})$ described in Section 2 to denote this data provenance code.

6.5. Relational Integrity

As described in Section 2, the data in each d*ion*t0*dt* file are self-contained to simplify and speed up the calculation of a wide variety of rates at runtime, but as a result, this scheme obviates the relational integrity of the database. For instance, the wavelengths displayed in file d*ion*t050 (see Figure 3) are not automatically recalculated if level energies are updated in file d*ion*t006 (Figure 2). The level attributes specified in the latter file are also repeated in several other data types, e.g., the K-vacancy level energy in file d*ion*t086 (Figure 4). The extent of this complication is further illustrated in the list of data types in Appendix A. Data type 14 lists the ionization potential for every ionic species, but this datum is also contained in the floating-point tuple of every level in data type 06. Some of the level integer attributes of the latter data type are included in data types dealing with the effective ion charge (57), photoionization cross-sections (49, 53, 85, and 88), superlevel recombination rates (70 and 99), and satellite-level autoionization rates (72).

This database model can therefore make updating an involved and error-prone process, which can be mitigated by adopting an SQL-based relational database engine and devising a utility to perform the transcription to the `atdb.fits` file. Despite the wide variety of data types (see Appendix A) and record lengths, this is possible as shown by the development of the `uaDB` database (see Section 8). However, this scheme would hamper the generation of new data types, which is central to the XSTAR data curation strategy (see Section 2), and also lead to a more voluminous `atdb.fits` file. This proposition is being considered in the XSTAR development roadmap.

6.6. Atomic Data Accuracy

As astronomical observations become ever more accurate (see, for example, Figure 1), the reliability of the atomic data used in spectral modeling is under recurrent scrutiny, and hence, data assessment activities are key. In this respect, we have seen three schemes: by a reputed institution such as NIST [92]; by appointed review panels (e.g., VAMDC [93]), and by an open community of both data producers and users (e.g., AtomPy [94]). Our research group comprises both computational atomic physicists and astrophysical modelers, so we favor the latter. However, it has not been easy to determine accuracy ratings in our datasets for K-line diagnostics (Section 3) due to the lack of laboratory measurements and

despite adopting a multi-code computational strategy. As described in Section 4, we have pursued benchmarks of the photoabsorption cross-sections using astronomical observations of ISM K absorption, but they led to a polemic between laboratory spectroscopists and observational astronomers that was fortunately settled.

We have mentioned in Section 2 that our main concern regarding the XSTAR database upgrade has been the complete datasets for K-shell processes in ions with $Z \leq 30$, at the expense of neglecting those for the valence-shell that in general imply data collection rather than new computations. It may be seen in Appendix C that most of the current datasets for valence-shell transitions go back to the original version [2] then demanding an extensive overhaul. This is one of our main priorities in the database curation.

7. ISMabs

Although the main components of the ISM are neutral ionic species, the also perceived existence of charged ions prompted us to develop a new ISM X-ray absorption model referred to as `ISMabs` [35]. It includes atomic data for singly and doubly ionized species of cosmically abundant elements, namely H, He, C, N, O, Ne, Mg, Si, S, Ar, Ca, and Fe, in addition to the neutral systems. This model allows ion column densities to be determined directly, and the inclusion of ionized species has led to improved spectral fits as compared to those only considering neutral systems. The completeness and accuracy of the relevant atomic data are crucial to avoid misidentification and misinterpretation of the absorption features detected in analyses of ISM X-ray absorption spectra relying on fits of Gaussian profiles. We have performed with this model a detailed study of X-ray absorption in the local ISM by analyzing spectra from 24 Galactic sources. We have estimated the fractions of neutral and singly and doubly ionized species of O, Ne, and Fe, confirming the dominance of the cold component and a pervasive low degree of ionization [36].

8. Universal Atomic Database (uaDB)

The collection of atomic data in XSTAR is comprised of data in many different formats from many different sources. To assist in disseminating these data to the larger community and to account for the addition of new data, the Universal Atomic Database (`uaDB`) was developed. The `uaDB` is a mySQL database hosted at NASA/GSFC, accessed via its website (https://heasarc.gsfc.nasa.gov/uadb/index.php), and data can be queried based on a number of properties such as ion and data type. The web page also contains tools to help assess what data are available across ions or data types. One such tool displays the type of data available on a grid of element vs. ion (see Figure 11) while another displays all atomic lines present in a given wavelength range.

The main features of `uaDB` are:

- Each dataset contains a reference to the source paper(s);
- Data are stored in the original format and units as published;
- Multiple entries can exist for the same quantity (e.g., theoretical vs. measured energy levels);
- The coupling scheme of atomic states is built into the database structure;
- Data collections exist that define a complete model; no duplicate data exist within a collection.

All data in `uaDB` have a reference to the data source. The reference consists of a link to the journal article where the data were obtained and to its entry in NASA/ADS. The user is never more than a couple mouse clicks away from reading the source article. Data are entered into `uaDB` in the same format and with the same units as published. This means that, for example, some energy levels are stored in eV and others in cm^{-1}. The `uaDB` understands these units and can internally convert them for data querying in an energy range. The `uaDB` can also convert between quantities that differ by a statistical weight (e.g., f-values and gf-values) since it understands the level structure. We do not modify published data in order to be as true as possible to the original source and to help identify transcription

errors. However, this can make it more difficult to compare data from different sources. To help compare data, tools are developed that can perform the necessary conversions.

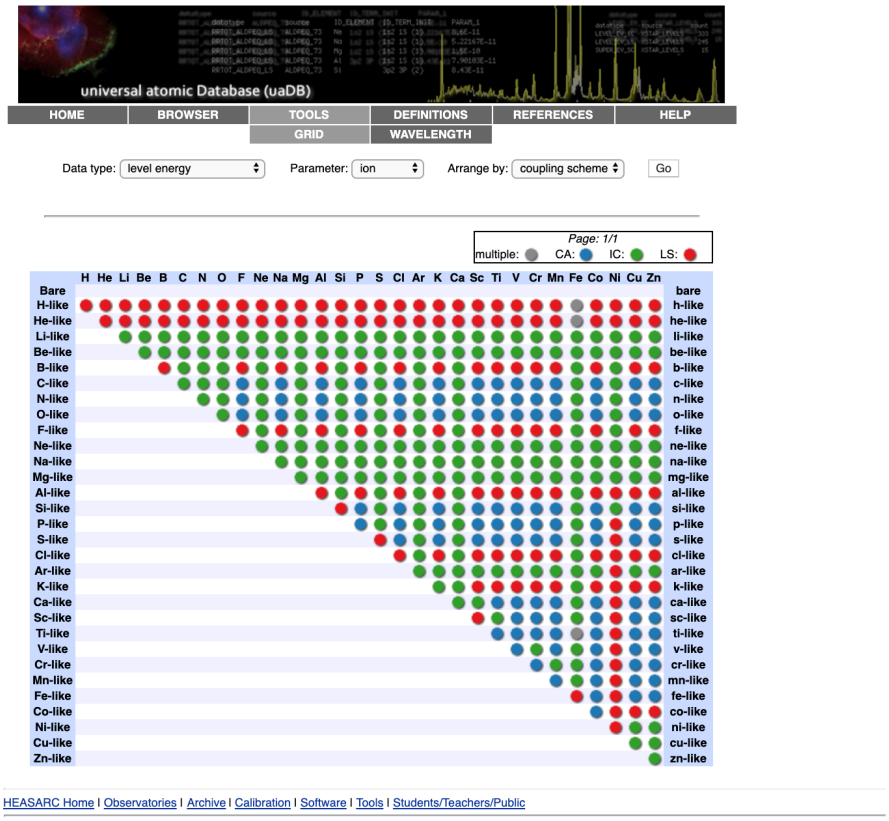

Figure 11. Grid tool in uaDB.

When compiling a set of atomic data for modeling purposes, it is important to have coverage; that is, for each state included in the model, a full set of data connecting that state with other states is necessary. If there are data allowing the population of a state to increase but no data to decrease it, then the model as a whole will be flawed. Furthermore, if the atomic model encompasses a large set of ions, it is difficult to obtain atomic data from the literature of equal quality. We often need to combine level-resolved data with term-resolved data to achieve coverage for an ion. To help with these difficulties, uaDB has different coupling schemes built into its structure and is aware of how different coupling schemes relate. Thus, when combining LS states with LSJ, uaDB can detect if any states are being double-counted. There are also routines for converting data from one coupling scheme to another based on simple statistical weighting.

The uaDB currently contains the complete set of data included in XSTAR as well as the level data from CHIANTI. To assist in distinguishing these data, uaDB defines collections. A collection is a dataset where there is no duplication of values for the same quantity. Currently, in uaDB the collection is just a label that can be used to constrain a query, but in the future collections could be created dynamically to construct a custom model. Collections are not part of the XSTAR development program, but have been widely used in, for instance, the PyNeb Python package to model emission lines in gaseous nebulae and, more recently, to assess atomic data accuracy [95,96].

9. Discussion and Conclusions

The present report describes in detail the updated version of the underlying atomic database of the XSTAR photoionization code to replace the original implementation of [2]. We include complete lists of the current rate types, data types (Appendix A), ionic models (Appendix B), and source references (Appendix C). We summarize the systematic calcula-

tions performed to characterize the metal K-lines for astronomical X-ray spectral modeling and recent extensions of the database, namely continuum lowering and dielectronic recombination suppression, to deal with high-density ($n_e \leq 10^{22}$ cm^{-3}) plasmas. We have tried to convey the intricacies in the development and maintenance of an application-based atomic database, which go way beyond the compilation of the data and lead to curatorial and integrity problems caused by the ever-increasing dataset volumes.

An important finding is that the atomic models used to compute the data are not necessarily suitable for plasma modeling, particularly for ionic species with electron number $N > 19$. Level-number trimming was necessary to implement functional atomic representations for such systems, although their soundness in non-LTE modeling deserves further attention as the appearance of unexpected metastable levels becomes an issue.

A further point worth emphasizing is that the XSTAR atomic database and output files are structured under the FITS format specifications, which has been established as the standard for astronomical datasets associated to the new generation of telescopes. We believe that this compliance will reduce user stress in intense data processing, which is bound to take place at the data repositories rather than locally.

We have briefly recounted two projects that have emerged from the XSTAR database, namely the `ISMabs` absorption model and the `uaDB` database. The former has become an important initiative as it has led to benchmarks of the atomic data with observations and laboratory measurements; however, it has not been a smooth process as unexpected inaccuracies in the calibration of the laboratory wavelength scale were detected and finally resolved [23,52]. This outcome has given us some confidence in the identification of the spectral features and the accuracy of our atomic data. The `uaDB` database model will be helpful in future projects to disseminate the larger atomic data volumes required in non-LTE modeling.

A question that remains unanswered is whether our efforts to ensure accuracy and completeness for the XSTAR database are sufficient to exploit the high resolution and sensitivity expected from the microcalorimeter-based spectrometers aboard the new X-ray space telescopes. The encouraging fit of the showcase HITOMI spectrum of Figure 1 required basic data manipulation, but at least it was conclusive. Therefore, we envision further database refinement in the near future, especially improved datasets for valence-shell processes, to provide a reliable modeling platform for high-resolution spectroscopy in the new era. In this respect more laboratory benchmarks would be welcome.

Author Contributions: Conceptualization, C.M., M.A.B. and T.R.K.; methodology, C.M., E.G., J.A.G., J.D., M.A.B., M.C.W., P.P., P.Q., T.R.K. and T.W.G.; software, C.M., E.G., J.A.G., M.A.B., M.C.W., P.P., T.R.K. and T.W.G.; validation, J.A.G., M.A.B., P.P. and T.R.K.; formal analysis, C.M., E.G., J.A.G., J.D., M.A.B., M.C.W., P.P., P.Q., T.R.K. and T.W.G.; investigation, C.M., E.G., J.A.G., J.D., M.A.B., M.C.W., P.P. and T.R.K.; validation, C.M., M.A.B., P.P. and T.R.K.; resources, M.A.B., P.Q. and T.R.K.; data curation, C.M., M.A.B., P.P. and T.R.K.; writing—original draft preparation, C.M., E.G., M.C.W. and T.R.K.; writing—review and editing, C.M., E.G., J.A.G., J.D., M.A.B., M.C.W., P.P., P.Q., T.R.K. and T.W.G.; visualization, C.M., M.C.W. and T.R.K.; supervision, T.R.K.; project administration, M.A.B., P.Q. and T.R.K.; funding acquisition, J.A.G., P.P., P.Q. and T.R.K. All authors have read and agreed to the published version of the manuscript.

Funding: J.D. is a Research Fellow of the Belgian Fund for Research in Industry and Agriculture (FRIA). P.P. & P.Q. are, respectively, Research Associate and Research Director of the Belgian Fund for Scientific Research F.R.S.–FNRS. Financial support from these organizations as well as from the NASA Astrophysics Research and Analysis Program (grants 12-APRA12-0070; 80NSSC17K0345; and 80NSSC19K0586) and the Alexander von Humboldt Foundation are gratefully acknowledged.

Data Availability Statement: The XSTAR modeling code, the `uaDB` database, and the `ISMabs` model are available from the website of the NASA High Energy Astrophysics Science Archive Research Center (HEASARC, https://heasarc.gsfc.nasa.gov/).

Acknowledgments: We are grateful to Anil. K. Pradhan (Ohio State University) for access to and space-time allocation at the Ohio Supercomputer Center and also to the NASA Private Cloud at GSFC for access and virtual machine installation, especially to Michael D. Moore for invaluable support.

Conflicts of Interest: The authors declare no conflict of interest.

Abbreviations

The following abbreviations are used in this manuscript:

ADAS	Atomic Data and Analysis Structure
ADS	Astrophysics Data System
ALS	Advanced Light Source
AMDPP	Atomic and Molecular Diagnostic Processes in Plasmas
FITS	Flexible Image Transport System
GSFC	Goddard Space Flight Center
HZB	Helmholtz-Zentrum Berlin
IPNAS	Institut de Physique Nucléaire, Atomique et de Spectrométrie
LTE	Local Thermodynamic Equilibrium
NASA	National Aeronautics and Space Administration
NIST	National Institute of Standards and Technology
PP95	Atomic Data for the Analysis of Emission Lines
SQL	Structured Query Language
WSRC	Wisconsin Synchrotron Radiation Center

Appendix A. Data Types

This appendix lists the data types of the XSTAR database. Unless otherwise stated, the temperature T is given in 10^4 K units. The record attributes are: `r1`, `r2`, ... for the real variables; `i1`, `i2`, ... for the integer variables; and `s1`, `s2`, ... for the character strings. The following notation is used: *ion* is the ion identifier; Z the atomic number; N the electron number; $E(\infty)$ the ionization potential; $E(i)$ the ith level energy; n the principal quantum number; ν the effective quantum number; S the total spin quantum number; L the total orbital angular momentum quantum number; J the total angular momentum quantum number; λ the radiative transition wavelength; $gf(i,k)$ the weighted oscillator strength; and $A(k,i)$ the transition rate.

01. Radiative recombination rate coefficient of N-electron recombined ion [89,97]: `r1` $= A_{\rm rad}$ (cm^3 s^{-1}); `r2` $= \eta$; `i1` $= ion_N$.

02. H^0 charge exchange rate coefficient of N-electron recombined ion [98]: `r1` $= a$ (10^{-9} cm^3 s^{-1}); `r2` $= b$; `r3` $= c$; `r4` $= d$; `r5` $= T_1$ (K); `r6` $= T_2$ (K); `r7` $= \Delta E/k$ (10^4 K); `i1` $= ion_N$; `s1` = recombining ion identifier.

06. Data attributes of the ith level of N-electron ion: `r1` $= E(i)$ (eV); `r2` $= (2J+1)$; `r3` $= \nu$ (effective quantum number); `r4` $= E(\infty)$ (eV); `i1` $= n$; `i2` $= (2S+1)$; `i3` $= L$; `i4` $= Z$; `i5` $= i$; `i6` $= ion_N$; `s1` = level assignment (electron configuration and spectroscopic term).

07. Dielectronic recombination rate coefficient of N-electron recombined ion [89,97]: `r1` $= A_{\rm di}$ (cm^3 s^{-1} K$^{3/2}$); `r2` $= B_{\rm di}$; `r3` $= T_0$; `r4` $= T_1$; `i1` $= ion_N$.

14. Ionization potential of N-electron ion: `r1` $= E(\infty)$ (eV); `i1` $= Z - N + 1$; `i2` $= Z$; `i3` $= ion_N$; `s1` = ion identifier.

22. Dielectronic recombination rate coefficient of the N-electron recombined ion [99]: `r1` $= a$; `r2` $= b$; `r3` $= c$; `r4` $= d$; `r5` $= f$; `i1` $= ion_N$.

30. Total radiative recombination rate (hydrogenic) for N-electron recombined ion [100]: `i1` $= Z$; `i2` $= ion_N$.

38. Total radiative recombination rate coefficient of N-electron recombined ion [http://amdpp.phys.strath.ac.uk/tamoc/DATA/RR/]: `r1` $= A$ (cm^3 s^{-1}); `r2` $= B$; `r3` $= T_0$ (K); `r4` $= T_1$ (K); `r5` $= C$; `r6` $= T_2$ (K); `i1` $= Z$; `i2` $= N - 1$; `i3` $= M$; `i4` $= W$; `i5` $= ion_N$.

39. Total dielectronic recombination rate coefficient of N-electron recombined ion [http://amdpp.phys.strath.ac.uk/tamoc/DATA/DR/]: $\texttt{r1}-\texttt{rj}_{\texttt{max}} = (C(j), j = 1, j_{\max})$ ($\mathrm{cm}^3\,\mathrm{s}^{-1}\,\mathrm{K}^{3/2}$); $\texttt{rj}_{\texttt{max}+1}-\texttt{rj}_{2*\texttt{max}} = (T(j), j = 1, j_{\max})$ (K); $\texttt{i1} = Z$; $\texttt{i2} = N - 1$; $\texttt{i3} = M$; $\texttt{i4} = W$, $\texttt{i5} = ion_N$.

49. Partial photoionization cross-section of i_Nth level of the N-electron ion leaving the $(N-1)$-electron ion in the k_{N-1}th level: $\texttt{r1}-\texttt{rj}_{2*\texttt{max}} = (E(j), \sigma(E(j)), j = 1, j_{\max})$ (Energy in Ryd relative to $E(\infty)$, cross-section in Mb); $\texttt{i1} = n$; $\texttt{i2} = L$; $\texttt{i3} = 2J$; $\texttt{i4} = Z$; $\texttt{i5} = k_{N-1}$; $\texttt{i6} = ion_{N-1}$; $\texttt{i7} = i_N$; $\texttt{i8} = ion_N$.

50. Line $(k - i)$ radiation rates of N-electron ion: $\texttt{r1} = \lambda$ (Å); $\texttt{r2} = gf(i,k)$; $\texttt{r3} = A(k,i)$ (s^{-1}); $\texttt{i1} = i$ (lower level); $\texttt{i2} = k$ (upper level); $\texttt{i3} = Z$; $\texttt{i4} = ion_N$.

51. Electron-impact effective collision strength for the $k - i$ transition of N-electron ion (CHIANTI fit [61,101]): $\texttt{r1} = \Delta E$ (Ryd); $\texttt{r2} = C$; $\texttt{r3}-\texttt{r7} = (\Upsilon_{\mathrm{red}}(j), j = 1, 5)$ (reduced effective collision strength); $\texttt{i1} = it$ (transition type); $\texttt{i2} = i$ (lower level); $\texttt{i3} = k$ (upper level); $\texttt{i4} = Z$; $\texttt{i5} = ion_N$.

53. TOPbase partial photoionization cross-section (resonance averaged) of i_Nth level of the N-electron ion leaving the $(N-1)$-electron ion in the k_{N-1}th level: $\texttt{r1}-\texttt{rj}_{2*\texttt{max}} = (E(j), \sigma(E(j)), j = 1, j_{\max})$ (Energy in Ryd relative to $E(\infty)$, cross-section in Mb); $\texttt{i1} = n$; $\texttt{i2} = L$; $\texttt{i3} = 2J$; $\texttt{i4} = Z$; $\texttt{i5} = k_{N-1}$; $\texttt{i6} = ion_{N-1}$; $\texttt{i7} = i_N$; $\texttt{i8} = ion_N$.

54. Radiative transition probability A_{ki} for the $k - i$ transition of N-electron ion computed by quantum defect theory (or hydrogenic): $\texttt{r1} = 0.0\mathrm{E}{+}0$; $\texttt{i1} = i$ (lower level); $\texttt{i2} = k$ (upper level); $\texttt{i3} = Z$; $\texttt{i4} = ion_N$.

56. Electron-impact effective collision strengths for the $k - i$ transition of N-electron ion: $\texttt{r1}-\texttt{rj}_{\texttt{max}} = (\log T_e(j), j = 1, j_{\max})$ (K); $\texttt{rj}_{(\texttt{max}+1)}-\texttt{rj}_{(2*\texttt{max})} = (\Upsilon(T_e(j)), j = 1, j_{\max})$ (effective collision strength); $\texttt{i1} = i$ (lower level); $\texttt{i2} = k$ (upper level); $\texttt{i3} = Z$; $\texttt{i4} = ion_N$.

57. Effective ion charge for ith level of N-electron ion used in collisional ionization rates: $\texttt{r1} = Z_{\mathrm{eff}}$; $\texttt{i1} = n$; $\texttt{i2} = L$; $\texttt{i3} = 2J$; $\texttt{i4} = i$; $\texttt{i5} = ion_N$

59. Partial photoionization cross-section of i_Nth level of the N-electron ion leaving the $(N-1)$-electron ion in the k_{N-1}th level [102]: $\texttt{r1} = E(th)$ (eV); $\texttt{r2} = E(0)$ (eV); $\texttt{r3} = \sigma(0)$ (Mb); $\texttt{r4} = y(a)$; $\texttt{r5} = P$; $\texttt{r6} = y(w)$; $\texttt{i1} = N$; $\texttt{i2} = n$ (shell principal quantum number); $\texttt{i3} = l$ (subshell orbital quantum number); $\texttt{i4} = k_{N-1}$; $\texttt{i5} = ion_{N-1}$; $\texttt{i6} = i_N$; $\texttt{i7} = ion_N$; $\texttt{s1}$ = shell–ion identifier.

60. Analytic fits for effective collision strengths in H-like ions [103]: $\texttt{r1}-\texttt{rj}_{\texttt{max}}$ = coefficients; $\texttt{i1} = i$ (lower level); $\texttt{i2} = k$ (upper level); $\texttt{i3} = nphot$; $\texttt{i4} = ion_N$; $\texttt{s1}$ = Transition.

62. Analytic fits for effective collision strengths in H-like ions [103]: $\texttt{r1}-\texttt{rj}_{\texttt{max}}$ = coefficients; $\texttt{i1} = i$ (lower level); $\texttt{i2} = k$ (upper level); $\texttt{i3} = 1$; $\texttt{i4} = ion_N$; $\texttt{s1}$ = Transition.

63. Collisional transition probability C_{ik} for N-electron ion computed by quantum defect theory (or hydrogenic): $\texttt{i1} = 1$ $\texttt{i2} = i$ (lower level); $\texttt{i3} = k$ (upper level); $\texttt{i4} = Z$; $\texttt{i5} = ion_N$.

66. Fits to fine-structure collision strengths for He-like ions [104]: $\texttt{r1}-\texttt{rj}_{\texttt{max}}$ = coefficients; $\texttt{i1} = i$ (lower level); $\texttt{i2} = k$ (upper level); $\texttt{i3} = Z$; $\texttt{i4} = ion_N$.

67. Analytic fits for effective collision strengths in He-like ions [105]: $\texttt{r1}-\texttt{rj}_{\texttt{max}}$ = coefficients; $\texttt{i1} = i$ (lower level); $\texttt{i2} = k$ (upper level); $\texttt{i3} = Z$; $\texttt{i4} = ion_N$.

68. Analytic fits for effective collision strengths in He-like ions [106]: $\texttt{r1}-\texttt{rj}_{\texttt{max}}$ = coefficients; $\texttt{i1} = i$ (lower level); $\texttt{i2} = k$ (upper level); $\texttt{i3} = Z$; $\texttt{i4} = ion_N$.

69. Fits to LS collision strengths for He-like ions [104]: $\texttt{r1}-\texttt{rj}_{\texttt{max}}$ = coefficients; $\texttt{i1} = i$ (lower level); $\texttt{i2} = k$ (upper level); $\texttt{i3} = Z$; $\texttt{i4} = ion_N$.

70. Coefficients for recombination and photoionization cross-sections of superlevels: $\texttt{r1}-\texttt{rj}_{\texttt{nd}} = (n_e(j), j = 1, j_{nd})$ (cm^{-3}); $\texttt{rj}_{\texttt{nd}+1}-\texttt{rj}_{\texttt{nd}+\texttt{nt}} = (T_e(j), j = 1, j_{nt})$; $\texttt{rj}_{\texttt{nd}+\texttt{nt}+1}-\texttt{rj}_{\texttt{nd}+\texttt{nt}+\texttt{nt}*\texttt{nd}} = ((\log \alpha(j, j'), j = 1, j_{nt}), j' = 1, j'_{nd})$; $\texttt{rj}_{\texttt{nd}+\texttt{nt}+\texttt{nt}*\texttt{nd}+1}-\texttt{rj}_{\texttt{nd}+\texttt{nt}+\texttt{nt}*\texttt{nd}+2*\texttt{nx}} = (E(j), \sigma(j), j = 1, j_{nx})$ (Ryd, Mb); $\texttt{i1} = nd$; $\texttt{i2} = nt$; $\texttt{i3} = nx$; $\texttt{i4} = n$; $\texttt{i5} = L$; $\texttt{i6} = 2S + 1$; $\texttt{i7} = Z$; $\texttt{i8} = k_{N-1}$; $\texttt{i9} = ion_{N-1}$; $\texttt{i10} = i_N$; $\texttt{i11} = ion_N$.

71. Radiative transition rates from superlevels to spectroscopic levels: $\texttt{r1}-\texttt{rj}_{\texttt{nd}} = (n_e(j), j = 1, j_{nd})$ (cm^{-3}); $\texttt{rj}_{\texttt{nd}+1}-\texttt{rj}_{\texttt{nd}+\texttt{nt}} = (T_e(j), j = 1, j_{nt})$; $\texttt{rj}_{\texttt{nd}+\texttt{nt}+1}-\texttt{rj}_{\texttt{nd}+\texttt{nt}+\texttt{nt}*\texttt{nd}} =$

$((A(j,j'),j=1,j_{nt}),j'=1,j'_{nd})$ (s^{-1}); $\texttt{r}_{\texttt{nd+nt+nt*nd+1}}=\lambda$ (Å); $\texttt{i1}=nd$; $\texttt{i2}=nt$; $\texttt{i3}=i$ (lower level); $\texttt{i4}=k$ (upper level); $\texttt{i5}=Z$; $\texttt{i6}=ion_N$.

72. Autoionization rates for satellite levels: $\texttt{r1}=A_a(k,i)$ (s^{-1}); $\texttt{r2}=E(k)$ (eV above ionization limit); $\texttt{r3}=(2J+1)$; $\texttt{i1}=(2S+1)$; $\texttt{i2}=L$; $\texttt{i3}=k$ (level); $\texttt{i4}=i$ (continuum level); $\texttt{i5}=Z$; $\texttt{i6}=ion_N$; $\texttt{s1}=$ level configuration.

73. Fit to effective collision strengths for satellite levels of He-like ions [107]: $\texttt{r1}-\texttt{r7}=$ fit coefficients; $\texttt{i1}=i$ (lower level); $\texttt{i2}=j$ (upper level); $\texttt{i3}=Z$; $\texttt{i4}=ion_N$.

74. Delta functions to add to photoionization cross-sections to match ADAS DR rates: $\texttt{r1}=E(\infty)$ (Ryd); $\texttt{r2}-\texttt{rj}_{\texttt{m+1}}=(E(j),j=1,j_m)$ (Ryd); $\texttt{rj}_{\texttt{m+2}}-\texttt{rj}_{\texttt{2*m+1}}=(f(j),j=1,j_m)$ (cm^2); $\texttt{i1}=n$; $\texttt{i2}=L$; $\texttt{i3}=2S+1$; $\texttt{i4}=Z$; $\texttt{i5}=k_{N-1}$; $\texttt{i6}=ion_{N-1}$; $\texttt{i7}=i_N$; $\texttt{i8}=ion_N$.

75. Autoionization rates for Fe XXIV satellites [5]: $\texttt{r1}=A_a(k,i)$ (s^{-1}); $\texttt{r2}=E(k)$ (eV above ionization limit); $\texttt{i1}=ion_N$, $\texttt{i2}=k_N$; $\texttt{i3}=ion_{N-1}$; $\texttt{i4}=i_{N-1}$; $\texttt{i5}=ion_N$.

76. Two-photon radiation rate for $(k-i)$ transition of N-electron ion: $\texttt{r1}=A(k,i)$ (s^{-1}); $\texttt{i1}=i$ (lower level); $\texttt{i2}=k$ (upper level); $\texttt{i3}=N$; $\texttt{i4}=ion_N$; $\texttt{s1}=$ transition.

77. Collision transition rates from superlevels to spectroscopic levels: $\texttt{r1}-\texttt{rj}_{\texttt{nd}}=(n_e(j),j=1,j_{nd})$ (cm^{-3}); $\texttt{rj}_{\texttt{nd+1}}-\texttt{rj}_{\texttt{nd+nt}}=(T_e(j),j=1,j_{nt})$; $\texttt{rj}_{\texttt{nd+nt+1}}-\texttt{rj}_{\texttt{nd+nt+nt*nd}}=((C(j,j'),j=1,j_{nt}),j'=1,j'_{nd})$ (s^{-1}); $\texttt{rj}_{\texttt{nd+nt+nt*nd+1}}=\lambda$ (Å); $\texttt{i1}=nd$; $\texttt{i2}=nt$; $\texttt{i3}=i$ (lower level); $\texttt{i4}=k$ (upper level); $\texttt{i5}=Z$; $\texttt{i6}=ion_N$.

81. Collision strengths for Fe XIX [108]: $\texttt{r1}=\Upsilon(k,i)$; $\texttt{i1}=i$ (lower level); $\texttt{i2}=k$ (upper level); $\texttt{i3}=Z$; $\texttt{i4}=ion_N$.

82. Decay rates for Fe UTA [109]: $\texttt{r1}=\lambda$ (Å); $\texttt{r2}=E(k)$ (eV); $\texttt{r3}=gf(i,k)$; $\texttt{r4}=A_r(k,i)$ (s^{-1}); $\texttt{r5}=A_a(k,i)$ (s^{-1}); $\texttt{i1}=i$ (lower level); $\texttt{i2}=k$ (upper level); $\texttt{i3}=ion_N$.

83. Level data for Fe UTA [109]: $\texttt{r1}=E(i)$ (eV); $\texttt{r2}=(2J+1)$; $\texttt{r3}=0.0$; $\texttt{r4}=0.0$; $\texttt{i1}=1$; $\texttt{i2}=i$ (level); $\texttt{i3}=ion_N$; $\texttt{s1}=$ level configuration assignment.

85. Photoionization cross-sections for Fe ions obtained by summation of resonances near the K edge [3]: $\texttt{r1}=Z_{\text{eff}}$; $\texttt{r2}=E_{th}$ (Ryd); $\texttt{r3}=f$; $\texttt{r4}=\gamma$; $\texttt{r5}=$ scaling factor; $\texttt{i1}=n$; $\texttt{i2}=L$; $\texttt{i3}=2J$; $\texttt{i4}=Z$; $\texttt{i5}=k_{N-1}$; $\texttt{i6}=ion_{N-1}$; $\texttt{i7}=i_N$; $\texttt{i8}=ion_N$.

86. Auger and radiative widths of k_Nth K-vacancy level: $\texttt{r1}=E(k_N)$ (eV, relative to $E(\infty)$); $\texttt{r2}=A_a(k_N)$ (s^{-1}); $\texttt{r3}=A_a(k_N,i_{N-1})$ (s^{-1}); $\texttt{r4}=A_r(k_N)$ (s^{-1}); $\texttt{i1}=i_{N-1}$; $\texttt{i2}=k_N$; $\texttt{i3}=Z$; $\texttt{i4}=ion_{N-1}$; $\texttt{i5}=ion_N$.

88. Photoionization cross-section damped excess of i_Nth level of the N-electron ion leaving the $(N-1)$-electron ion in superlevel_[K] k_{N-1}: $\texttt{r1}-\texttt{rj}_{\texttt{2*max}}=(E(j),\sigma(E(j)),j=1,j_{\text{max}})$ (Energy in Ryd relative to $E(\infty)$, cross-section in Mb); $\texttt{i1}=n$; $\texttt{i2}=L$; $\texttt{i3}=2J$; $\texttt{i4}=Z$; $\texttt{i5}=k_{N-1}$; $\texttt{i6}=i_N$; $\texttt{i7}=ion_N$.

91. APED line $(k-i)$ radiation rates [110]: $\texttt{r1}=\lambda$ (Å); $\texttt{r2}=0.0$; $\texttt{r3}=A(k,i)$ (s^{-1}); $\texttt{i1}=i$ (lower level); $\texttt{i2}=k$ (upper level); $\texttt{i3}=Z$; $\texttt{i4}=ion_N$.

92. APED collision strengths [110]: $\texttt{r1}=T_e(1)$ (K); $\texttt{r2}=T_e(j_{max})$ (K); $\texttt{r3}-\texttt{rj}_{\texttt{max+2}}=(T_e(j),j=1,j_{max})$ (K); $\texttt{rj}_{\texttt{max+3}}-\texttt{rj}_{\texttt{2*max+2}}=(\Upsilon(j),j=1,j_{max})$; $\texttt{i1}=i$ (lower level); $\texttt{i2}=k$ (upper level); $\texttt{i3}=113$; $\texttt{i4}=Z$; $\texttt{i5}=ion_N$.

95. Collisional ionization rates for N-electron ion [111]: $\texttt{r1}=E(th)$ (eV); $\texttt{r2}=T_0$ (K); $\texttt{r3}-\texttt{rj}_{\texttt{max+2}}=(\rho(j),j=1,j_{max})$ (effective collision strength); $\texttt{i1}=i$ (level); $\texttt{i5}=ion_N$.

98. Electron-impact effective collision strengths for the $k-i$ transition of the N-electron ion (CHIANTI fit [61,101]): $\texttt{r1}=\Delta E$ (Ryd); $\texttt{r2}=C$; $\texttt{r3}-\texttt{rj}_{\texttt{max+2}}=(\Upsilon_{\text{red}}(j),j=1,j_{max})$ (reduced effective collision strength); $\texttt{i1}=i$; $\texttt{i2}=k$; $\texttt{i3}=it$ (transition type); $\texttt{i4}=ion_N$.

99. Coefficients for recombination and photoionization cross-sections of superlevels: $\texttt{r1}-\texttt{rj}_{\texttt{nd}}=(n_e(j),j=1,j_{nd})$ (cm^{-3}); $\texttt{rj}_{\texttt{nd+1}}-\texttt{rj}_{\texttt{nd+nt}}=(T_e(j),j=1,j_{nt})$; $\texttt{rj}_{\texttt{nd+nt+1}}-\texttt{rj}_{\texttt{nd+nt+nt*nd}}=((\alpha(j,j'),j=1,j_{nt}),j'=1,j'_{nd})$; $\texttt{rj}_{\texttt{nd+nt+nt*nd+1}}-\texttt{rj}_{\texttt{nd+nt+nt*nd+2*nx}}=(E(j),\sigma(j),j=1,j_{nx})$ (Ryd, Mb); $\texttt{i1}=nd$; $\texttt{i2}=nt$; $\texttt{i3}=nx$; $\texttt{i4}=n$; $\texttt{i5}=L$; $\texttt{i6}=2S+1$; $\texttt{i7}=Z$; $\texttt{i8}=k_{N-1}$; $\texttt{i9}=ion_{N-1}$; $\texttt{i10}=i_N$; $\texttt{i11}=ion_N$.

Appendix B. Ion Models

Table A1. Number of energy levels included in the XSTAR ion models.

N \ Z	1	2	3	4	5	6	7	8	9	10	11	12	13	14	15
1	33	33	33	33	33	33	33	33	33	33	33	33	33	33	33
2		46	32	32	32	56	58	241	52	54	52	58	52	58	52
3			3	3	3	26	43	43	22	43	22	43	22	43	22
4				3	3	22	53	53	43	79	43	79	43	79	43
5					3	22	58	163	53	163	53	163	53	163	53
6						8	61	79	53	79	53	79	53	79	53
7							82	34	34	34	34	34	63	34	34
8								19	3	19	19	19	57	19	19
9									3	118	7	7	7	7	7
10										4	3	46	46	46	50
11											3	24	4	60	42
12												3	4	57	31
13													3	18	55
14														3	3
15															3

N \ Z	16	17	18	19	20	21	22	23	24	25	26	27	28	29	30
1	33	33	33	33	33	33	33	33	33	33	33	33	33	33	33
2	58	52	38	52	46	52	52	52	52	52	50	52	43	52	52
3	43	22	43	22	43	22	22	22	22	22	52	22	53	22	22
4	79	43	79	43	79	43	43	43	43	43	199	43	79	43	43
5	163	53	163	53	163	53	53	53	53	53	551	53	163	53	53
6	79	53	53	53	53	53	53	53	53	53	623	53	53	53	53
7	34	34	34	34	34	34	34	34	34	34	744	34	34	34	34
8	19	19	19	19	29	19	19	19	19	19	639	19	67	19	19
9	7	7	7	7	7	7	7	7	7	7	340	7	117	7	7
10	46	50	72	50	78	50	50	50	50	50	276	50	98	50	50
11	60	42	208	42	208	42	42	42	42	42	85	42	216	42	42
12	53	31	153	31	149	31	31	31	31	31	146	31	171	31	31
13	76	55	208	55	208	55	55	55	55	55	55	55	235	55	55
14	82	71	249	71	249	71	71	71	71	71	68	71	269	71	71
15	31	55	211	55	211	55	55	55	55	55	78	55	219	55	55
16	3	3	143	31	143	31	31	31	31	31	70	31	145	31	31
17		3	62	10	62	10	10	10	10	10	62	10	63	10	10
18			3	3	3	54	54	54	54	54	31	54	40	54	54
19				3	5	221	221	221	221	221	170	221	143	221	221
20					3	32	258	258	258	258	54	258	258	258	258
21						3	84	441	441	441	55	441	441	441	441
22							3	3	537	537	33	537	537	537	537
23								3	163	463	70	463	463	463	463
24									3	160	73	295	295	295	295
25										3	197	128	128	128	128
26											3	3	40	40	40
27												3	3	3	3
28													3	3	3
29														3	3
30															3

Appendix C. Atomic Data Provenance

Table A2. Data provenance including the CHIANTI [61], PP95 [63], and AMDPP [64,65] compilations. rt = rate type. dt = data type.

ID	Code	rt	dt	(Z; N)	References
ac81	1000	3	56	(8; 1)	[112]
ac92	1001	3	56	(2; 1)	[113]
ak91	1002	3	56	(6; 1)	[114]
ak91a	1003	3	56	(10; 1)	[115]
ak92	1004	3	56	(14; 1)	[116]
ak92a	1005	3	56	(20; 1)	[117]
ak93	1006	3	56	(26; 1)	[118]
ba00	1007	4	50	(28; 2)	[91]
bm98	1008	3	56	(26; 15)	[119], CHIANTI ([120,121])
bn00	1009	3	56	(26; 20)	[122], CHIANTI ([123])
bp98	1010	3	56	(26; 25)	[90]
ch00	1011	3	51	(10; 7), (20; 8), (26; 16), (28; 14)	CHIANTI
ch00	1012	4	50	(6, 7, 8; 4), (12, 14; 5),(20; 8), (26; 6, 12, 14−18), (28; 14)	CHIANTI
ch01	1013	3	51	(6, 7; 3)	CHIANTI ([124])
ch01	1014	4	50	(6, 7; 3)	CHIANTI ([125,126])
ch02	1015	4	50	(8, 10, 12, 14, 16, 18, 20, 26, 28; 3)	CHIANTI ([126,127])
ch02	1016	3	51	(8, 10, 12, 14, 16, 18, 20, 28; 3)	CHIANTI ([127])
ch04	1017	3	51	(6; 4)	CHIANTI ([128,129])
ch04	1018	4	50	(10, 12, 16; 4)	CHIANTI ([130–132])
ch05	1019	3	51	(7; 4)	CHIANTI ([133])
ch05	1020	4	50	(14, 18, 26; 4)	CHIANTI, CHIANTI ([131])
ch06	1021	3	51	(8; 4)	CHIANTI ([132,134])
ch06	1022	4	50	(20, 28; 4)	CHIANTI ([130,132])
ch07	1023	3	51	(10, 12, 14, 16, 18, 20, 26, 28; 4)	CHIANTI ([131,132])
ch07	1024	4	50	(6; 5)	CHIANTI ([135–137]), NIST
ch08	1025	3	51	(6; 5)	CHIANTI ([138])
ch08	1026	4	50	(7; 5)	CHIANTI ([139,140])
ch09	1027	4	50	(8, 10; 5)	CHIANTI ([135])
ch09	1028	3	51	(7; 5)	CHIANTI ([141,142])
ch10	1029	4	50	(16, 18, 20; 5)	CHIANTI ([135,143])
ch10	1030	3	51	(8, 10, 12, 14, 16, 18, 20, 26; 5)	CHIANTI ([144])
ch11	1031	3	51	(28; 5)	CHIANTI ([145])
ch11	1032	4	50	(26; 5)	CHIANTI ([145])
ch12	1033	4	50	(28; 5)	CHIANTI ([135,143,145])
ch12	1034	3	51	(7; 6)	CHIANTI ([141,142])
ch13	1035	4	50	(7; 6)	CHIANTI, CHIANTI ([146])
ch13	1036	3	51	(8; 6)	CHIANTI ([147–150])
ch14	1037	4	50	(8; 6)	CHIANTI ([149])
ch14	1038	3	51	(10; 6)	CHIANTI ([150–152])
ch15	1039	4	50	(10, 12, 14; 6)	CHIANTI ([152,153])
ch15	1040	3	51	(12; 6)	CHIANTI ([154])
ch16	1041	3	51	(14; 6)	CHIANTI ([152,153]
ch16	1042	4	50	(16; 6)	CHIANTI ([155])
ch17	1043	4	50	(18; 6)	CHIANTI ([156]
ch17	1044	3	51	(16; 6)	CHIANTI ([155,157])
ch18	1045	3	51	(18; 6)	CHIANTI ([156])
ch18	1046	4	50	(20; 6)	CHIANTI ([158])
ch19	1047	3	51	(20; 6)	CHIANTI ([159,160])
ch19	1048	4	50	(12, 14, 16, 18, 20; 7)	CHIANTI ([161])
ch20	1049	4	50	(26; 7)	CHIANTI ([162])
ch20	1050	3	51	(26; 6)	CHIANTI ([163,164])
ch21	1051	4	50	(14, 16, 18; 8)	CHIANTI ([165])
ch21	1052	3	51	(8; 7)	CHIANTI ([166])

Table A2. *Cont.*

ID	Code	rt	dt	(Z; N)	References
ch22	1053	3	51	(12, 14, 16, 18, 20; 7)	CHIANTI ([161])
ch22	1054	4	50	(26; 8)	CHIANTI ([167])
ch23	1055	3	51	(26; 7)	CHIANTI ([161,162])
ch24	1056	4	50	(12, 14, 16, 20; 9)	CHIANTI ([168]), NIST
ch24	1057	3	51	(10, 12; 8)	CHIANTI ([169])
ch25	1058	3	51	(14, 16, 18; 8)	CHIANTI ([165])
ch25	1059	4	50	(26, 28; 9)	CHIANTI ([168,170,171]), NIST
ch26	1060	4	50	(14; 10)	CHIANTI ([172])
ch26	1061	3	51	(26; 8)	CHIANTI ([167])
ch27	1062	4	50	(16; 10)	CHIANTI ([173])
ch27	1063	3	51	(10; 9)	CHIANTI ([174])
ch28	1064	3	51	(12; 9)	CHIANTI ([174,175])
ch28	1065	4	50	(18, 20, 28; 10)	CHIANTI ([173,176])
ch29	1066	4	50	(26; 10)	CHIANTI ([177])
ch29	1067	3	51	(14; 9)	CHIANTI ([174,178])
ch30	1068	3	51	(16; 9)	CHIANTI ([174,179])
ch30	1069	4	50	(12, 14, 16, 18, 20, 26, 28; 11)	CHIANTI ([125,180])
ch31	1070	4	50	(14; 12)	CHIANTI, CHIANTI ([181])
ch31	1071	3	51	(20, 26; 9)	CHIANTI ([174,182])
ch32	1072	3	51	(14; 10)	CHIANTI ([172])
ch32	1073	4	50	(16, 18, 20, 28; 12)	CHIANTI ([183]), NIST
ch33	1074	4	50	(14; 13)	CHIANTI, CHIANTI ([184])
ch33	1075	3	51	(16; 10)	CHIANTI ([185])
ch34	1076	4	50	(16; 13)	CHIANTI ([186,187])
ch34	1077	3	51	(18, 20, 28; 10)	CHIANTI ([176])
ch35	1078	3	51	(26; 10)	CHIANTI ([177])
ch35	1079	4	50	(26; 13)	CHIANTI ([188])
ch36	1080	4	50	(26; 19)	CHIANTI ([189,190]), NIST
ch36	1081	3	51	(12, 14, 16, 18, 20, 28; 11)	CHIANTI ([180])
ch37	1082	3	51	(14; 12)	CHIANTI ([191])
ch37	1083	4	50	(26; 20)	CHIANTI ([192])
ch38	1084	3	51	(16, 18, 20, 28; 12)	CHIANTI ([183])
ch39	1085	3	51	(14; 13)	CHIANTI ([193])
ch40	1086	3	51	(16; 13)	CHIANTI ([186,187,194])
ch41	1087	3	51	(26; 18)	CHIANTI ([195,196])
ch42	1088	3	51	(26; 19)	CHIANTI ([189,197])
ch43	1089	3	51	(26; 14)	CHIANTI ([196,198])
cj94	1090	3	56	(1; 1)	[103,199]
cp99	1091	4	50	(26; 21)	[200]
cp99	1092	3	56	(26; 21)	[200]
eg99	1093	3	56	(26; 11)	[180,201]
ei99	1094	3	56	(26; 12)	CHIANTI, [202]
fe01	1095	4	50	(26; 25)	[203–206]
fe10	1096	3	56	(26; 17)	CHIANTI, [207]
fe24	1097	3	56	(26; 3)	[127,208]
gr58	1098	4	50	(26; 23)	[209]
im	1099	3	63	(7, 12, 16, 18, 28; 1), (7; 2)	Impact parameter method
kh84	1100	4	50	(2; 2)	[210]
km87	1101	3	56	(10, 14, 16; 2)	[105–107,211]
kn89	1102	3	69	(6; 2)	[104]
kn89b	1103	3	69	(2, 8, 12, 20; 2)	[104,107,211]
kn89c	1104	3	69	(26; 2)	[104–107,211]
mg05	1105	4	50	(12; 8)	PP95 ([212]), [213,214]
ne01	1106	4	50	(10; 7)	CHIANTI, PP95 ([212,215])
ne02	1107	4	50	(10; 8)	CHIANTI, PP95 ([212,214])
np96	1108	4	50	(26; 24)	[216]
ny01	1109	4	50	(7; 7)	[217–219]

Table A2. *Cont.*

ID	Code	rt	dt	(Z; N)	Reference
ox01	1110	4	50	(8; 6)	PP95 ([212,220]), CHIANTI ([149])
ox02	1111	4	50	(8; 7)	CHIANTI, PP95 ([212,215])
ox03	1112	4	50	(8; 8)	[218,219], PP95 ([212,214]
pb95	1113	3	56	(18, 20; 17)	[207]
pp01	1114	4	50	(6; 6)	PP95 ([136,212,213])
pp01	1115	3	56	(6; 6)	PP95 ([221–223])
pp02	1116	3	56	(7; 7)	PP95 ([224,225])
pp03	1117	3	56	(8; 8)	PP95 ([225,226])
pp04	1118	3	56	(16; 14)	PP95 ([214])
pp05	1119	4	50	(18, 20; 16)	PP95 ([212,214])
pp05	1120	3	56	(18; 14), (20; 19)	PP95 ([214])
pp06	1121	3	56	(18; 15)	PP95 ([227])
pp06	1122	4	50	(10; 9), (20; 17)	PP95 ([212])
pp07	1123	3	56	(18, 20; 16)	PP95 ([228])
pp07	1124	4	50	(16; 14)	PP95 ([212,229,230])
pp08	1125	4	50	(18; 15)	PP95 ([212,231])
pp09	1126	4	50	(18; 17)	PP95 ([214])
pp10	1127	4	50	(20; 19)	PP95 ([232])
pp11	1128	4	50	(18; 14)	PP95 ([187,212])
rb96	1129	3	56	(16; 15)	[233], CHIANTI ([234])
sm00	1130	3	51	(26; 13)	[235]
ss01	1131	4	50	(16; 15)	CHIANTI
ss96	1132	3	56	(18, 20; 13)	[236]
tb93	1133	4	50	(6, 7, 8, 10, 12, 14, 16, 18, 20, 26; 2)	[60]
zh96	1134	3	56	(26; 24)	[237]
zp97	1135	3	56	(26; 23)	[238]
zs87	1136	3	56	(18, 28; 2)	[106]
bm01	1137	3	56	(26; 3)	[5]
bm01	1138	4	50	(26; 3)	[5]
bm02	1139	3	56	(26; 4−10)	[8]
pm01	1140	4	50	(26; 2−9)	[6]
pm02	1141	4	50	(26; 18−25)	[7]
mk01	1142	4	50	(26; 10−17)	[9]
gm01	1143	4	50	(8; 2−8)	[11]
gk01	1144	4	50	(7; 1−7)	[17]
pm03	1145	4	50	(16; 2−16)	[14]
pq01	1146	4	50	(10, 12, 14, 16, 18, 20; 2−Z)	[15]
pq02	1147	4	50	(28; 2−27)	[16]
pq03	1148	4	50	(14; 2−13)	[22]
pq04	1149	4	50	(9, 11, 15, 17, 19; 2−(Z − 1)) (21−25, 27, 29, 30; 2−(Z − 1))	[26]
mb01	1150	3	56	(9, 11, 15, 17, 19, 21−25, 27; 3−(Z − 2)), (28; 19−26), (29, 30; 3−26)	Unpublished
fj01	1151	3	56	(26; 2, 3)	[110]
fj01	1152	4	50	(26; 2, 3)	[110]
gu01	1153	4	50	(26; 11−21)	[109]
gu01	1154	13	6	(26; 11−21)	[109]
kf01	1155	5	25	(3−5, 21, 29, 30; 2), (6−8, 16; (Z − 3)−Z), (10, 12, 14, 16, 18; (Z − 2)−Z), (26, 28; (Z − 2)−Z), (20; (Z − 1)−Z)	[98]
bb01	1156	5, 15	95	(1−30; 1−Z)	[111]
tb01	1157	7	53	(1−30; 1), (21−25, 27−30; 2), (28; 3−10, 21−26, 28)	Hydrogenic
tb02	1158	7	53	(2−20, 26; 2)	[239]
tb03	1159	7	53	(6, 7, 8, 10, 12, 14, 16, 18, 20, 26; 3)	[240]
tb04	1160	7	53	(6, 7, 8, 10, 12, 14, 16, 18, 20, 26; 4)	[241]

Table A2. *Cont.*

ID	Code	rt	dt	(Z;N)	Reference
tb05	1161	7	53	(6,7,8,10,12,14,16,18,20,26;5)	[242]
tb06	1162	7	53	(6,7,8,10,12,14,16,18,20,26;6)	[243]
tb07	1163	7	53	(7,8,10,12,14,16,18,20,26;7)	[60]
tb08	1164	7	53	(8,10,12,14,16,18,20,26;8)	[60]
tb09	1165	7	53	(10,12,14,16,18,20,26;9)	[60]
tb10	1166	7	53	(10,12,14,16,18,20,26;10)	[244]
tb11	1167	7	53	(14,18,20,26;11)	[60]
tb12	1168	7	53	(26;12)	[245]
tb13	1169	7	53	(26;13)	[246]
tb14	1170	7	53	(14,26;14)	[60,247]
tb15	1171	7	53	(16;16), (18;18), (26;15−21)	[60]
tb16	1172	7	53	(26;22)	[248]
tb17	1173	7	53	(26;23)	[249]
tb18	1174	7	53	(26;24)	[250]
tb19	1175	7	53	(26;25)	[251]
tb20	1176	7	53	(26;26)	[252]
tb21	1177	7	53	(28;27)	[218]
vy01	1178	1, 7	59	(3,4,5,9,11,15,17,19,21−25;1−Z), (27,29,30;1−Z), (13;1,2,12,13), (14;14), (16;16), (18;18), (20;18,19,20), (26;19−25), (28;21−28)	[102]
kp01	1179	7	53	(26;3−26)	[3,5,8,10]
gg01	1180	7	53	(6;3−6)	[21,37]
gm01	1181	7	53	(8;3−8)	[11]
gg02	1182	7	49	(8;6−8)	[23,32,33]
gk01	1183	7	53	(7;3−7)	[17]
wk01	1184	7	49	(10,12,14,16,18,20;3−10)	[18]
gg03	1185	7	49	(10;8−10)	[13,35,253]
wk02	1186	7	49	(12,14,16,18,20;11−17)	[19]
gg04	1187	7	49	(12;3−12)	[25]
wk03	1188	7	49	(13;3−11)	[24]
wk04	1189	7	49	(28;3−20)	[20]
tr01	1190	7	49	(9,11;3−(Z − 2)), (15,17,19;3−11) (21−25,27,29,30;3−11)	[27]
tr02	1191	7	49	(15,17,19;12−(Z − 2)), (21−25,27,29,30;12−18)	[28]
tr03	1192	7	49	(21−25,27;19−(Z − 2)), (28;21−26), (29,30;19−26)	[29]
ap01	1193	8	1	(3−30;2), (15−30;14−Z)	[89,97]
ap01	1194	8	7	(3−5;2−Z), (7,21,29,30;2), (13−25,27−30;13−Z)	[89,97]
ad01	1195	8	38	(3−12;3−Z), (13−30;3−13)	AMDPP ([65])
ad01	1196	8	39	(3−13;3−Z), (14−30;3−12), (26,28;13−20), (26;21−26)	AMDPP ([64])
ns01	1197	8	22	(13;13), (14;13,14)	[99]
gt01	1198	8	30	(1−30;1)	[100]

References

1. Kallman, T.; Bautista, M. Photoionization and High-Density Gas. *Astrophys. J. Suppl. Ser.* **2001**, *133*, 221–253. [CrossRef]
2. Bautista, M.A.; Kallman, T.R. The XSTAR Atomic Database. *Astrophys. J. Suppl. Ser.* **2001**, *134*, 139–149. [CrossRef]
3. Palmeri, P.; Mendoza, C.; Kallman, T.R.; Bautista, M.A. On the Structure of the Iron K Edge. *Astrophys. J.* **2002**, *577*, L119–L122. [CrossRef]
4. Palmeri, P.; Mendoza, C.; Kallman, T.; Bautista, M. Photoionization of the Fe Ions: Structure of the K-Edge. In *X-ray and Inner-Shell Processes*; Bianconi, A., Marcelli, A., Saini, N.L., Eds.; American Institute of Physics: College Park, MD, USA, 2003; AIP Conf. Proc. Volume 652; pp. 159–164. [CrossRef]
5. Bautista, M.A.; Mendoza, C.; Kallman, T.R.; Palmeri, P. Atomic data for the K-vacancy states of Fe XXIV. *Astron. Astrophys.* **2003**, *403*, 339–355. [CrossRef]

6. Palmeri, P.; Mendoza, C.; Kallman, T.R.; Bautista, M.A. A complete set of radiative and Auger rates for K-vacancy states in Fe XVIII-Fe XXV. *Astron. Astrophys.* **2003**, *403*, 1175–1184. [CrossRef]
7. Palmeri, P.; Mendoza, C.; Kallman, T.R.; Bautista, M.A.; Meléndez, M. Modeling of iron K lines: Radiative and Auger decay data for Fe II-Fe IX. *Astron. Astrophys.* **2003**, *410*, 359–364. [CrossRef]
8. Bautista, M.A.; Mendoza, C.; Kallman, T.R.; Palmeri, P. K-shell photoionization and electron impact excitation of Fe XVII-Fe XXIII. *Astrophys. J. Suppl. Ser.* **2004**, *418*, 1171–1178. [CrossRef]
9. Mendoza, C.; Kallman, T.R.; Bautista, M.A.; Palmeri, P. Decay properties of K-vacancy states in Fe X-Fe XVII. *Astron. Astrophys.* **2004**, *414*, 377–388. [CrossRef]
10. Kallman, T.R.; Palmeri, P.; Bautista, M.A.; Mendoza, C.; Krolik, J.H. Photoionization Modeling and the K Lines of Iron. *Astrophys. J. Suppl. Ser.* **2004**, *155*, 675–701. [CrossRef]
11. García, J.; Mendoza, C.; Bautista, M.A.; Gorczyca, T.W.; Kallman, T.R.; Palmeri, P. K-Shell Photoabsorption of Oxygen Ions. *Astrophys. J. Suppl. Ser.* **2005**, *158*, 68–79. [CrossRef]
12. Palmeri, P.; Kallman, T.R.; Mendoza, C.; Bautista, M.A.; Krolik, J.H. Photoionization Modeling: the K Lines and Edges of Iron. In *X-ray Diagnostics of Astrophysical Plasmas: Theory, Experiment, and Observation*; Smith, R., Ed.; American Institute of Physics: College Park, MD, USA, 2005; AIP Conf. Proc. Volume 774; pp. 75–82. [CrossRef]
13. Juett, A.M.; Schulz, N.S.; Chakrabarty, D.; Gorczyca, T.W. High-Resolution X-ray Spectroscopy of the Interstellar Medium. II. Neon and Iron Absorption Edges. *Astrophys. J.* **2006**, *648*, 1066–1078. [CrossRef]
14. Palmeri, P.; Mendoza, C.; Bautista, M.A.; García, J.; Kallman, T.R. K lines in the sulphur isonuclear sequence. *Rad. Phys. Chem.* **2006**, *75*, 1465–1470. [CrossRef]
15. Palmeri, P.; Quinet, P.; Mendoza, C.; Bautista, M.A.; García, J.; Kallman, T.R. Radiative and Auger Decay of K-Vacancy Levels in the Ne, Mg, Si, S, Ar, and Ca Isonuclear Sequences. *Astrophys. J. Suppl. Ser.* **2008**, *177*, 408–416. [CrossRef]
16. Palmeri, P.; Quinet, P.; Mendoza, C.; Bautista, M.A.; García, J.; Witthoeft, M.C.; Kallman, T.R. Radiative and Auger Decay Data for Modeling Nickel K Lines. *Astrophys. J. Suppl. Ser.* **2008**, *179*, 542–552. [CrossRef]
17. García, J.; Kallman, T.R.; Witthoeft, M.; Behar, E.; Mendoza, C.; Palmeri, P.; Quinet, P.; Bautista, M.A.; Klapisch, M. Nitrogen K-Shell Photoabsorption. *Astrophys. J. Suppl. Ser.* **2009**, *185*, 477–485. [CrossRef]
18. Witthoeft, M.C.; Bautista, M.A.; Mendoza, C.; Kallman, T.R.; Palmeri, P.; Quinet, P. K-Shell Photoionization and Photoabsorption of Ne, Mg, Si, S, Ar, and Ca. *Astrophys. J. Suppl. Ser.* **2009**, *182*, 127–130. [CrossRef]
19. Witthoeft, M.C.; García, J.; Kallman, T.R.; Bautista, M.A.; Mendoza, C.; Palmeri, P.; Quinet, P. K-shell Photoionization of Na-like to Cl-like Ions of Mg, Si, S, Ar, and Ca. *Astrophys. J. Suppl. Ser.* **2011**, *192*, 7. [CrossRef]
20. Witthoeft, M.C.; Bautista, M.A.; García, J.; Kallman, T.R.; Mendoza, C.; Palmeri, P.; Quinet, P. K-shell Photoionization of Nickel Ions using R-matrix. *Astrophys. J. Suppl. Ser.* **2011**, *196*, 7. [CrossRef]
21. Hasoglu, M.F.; Abdel-Naby, S.A.; Gorczyca, T.W.; Drake, J.J.; McLaughlin, B.M. K-shell Photoabsorption Studies of the Carbon Isonuclear Sequence. *Astrophys. J.* **2010**, *724*, 1296–1304. [CrossRef]
22. Palmeri, P.; Quinet, P.; Mendoza, C.; Bautista, M.A.; García, J.; Witthoeft, M.C.; Kallman, T.R. Atomic decay data for modeling the Al K lines. *Astron. Astrophys.* **2011**, *525*, A59. [CrossRef]
23. Gorczyca, T.W.; Bautista, M.A.; Hasoglu, M.F.; García, J.; Gatuzz, E.; Kaastra, J.S.; Kallman, T.R.; Manson, S.T.; Mendoza, C.; Raassen, A.J.J.; et al. A Comprehensive X-ray Absorption Model for Atomic Oxygen. *Astrophys. J.* **2013**, *779*, 78. [CrossRef]
24. Witthoeft, M.C.; Bautista, M.A.; García, J.; Kallman, T.R.; Mendoza, C.; Palmeri, P.; Quinet, P. Photoionization and photoabsorption cross sections for the aluminum iso-nuclear sequence. *At. Data Nucl. Data Tables* **2013**, *99*, 53–61. [CrossRef]
25. Hasoğlu, M.F.; Abdel-Naby, S.A.; Gatuzz, E.; García, J.; Kallman, T.R.; Mendoza, C.; Gorczyca, T.W. K-shell Photoabsorption of Magnesium Ions. *Astrophys. J. Suppl. Ser.* **2014**, *214*, 8. [CrossRef]
26. Palmeri, P.; Quinet, P.; Mendoza, C.; Bautista, M.A.; García, J.; Witthoeft, M.C.; Kallman, T.R. Atomic decay data for modeling K lines of iron peak and light odd-Z elements. *Astron. Astrophys.* **2012**, *543*, A44. [CrossRef]
27. Palmeri, P.; Quinet, P.; Mendoza, C.; Bautista, M.A.; Witthoeft, M.C.; Kallman, T.R. K-shell photoabsorption and photoionisation of trace elements. I. Isoelectronic sequences with electron number $3 \leq N \leq 11$. *Astron. Astrophys.* **2016**, *589*, A137. [CrossRef]
28. Mendoza, C.; Bautista, M.A.; Palmeri, P.; Quinet, P.; Witthoeft, M.C.; Kallman, T.R. K-shell photoabsorption and photoionization of trace elements. II. Isoelectronic sequences with electron number $12 \leq N \leq 18$. *Astron. Astrophys.* **2017**, *604*, A63. [CrossRef]
29. Mendoza, C.; Bautista, M.A.; Palmeri, P.; Quinet, P.; Witthoeft, M.C.; Kallman, T.R. K-shell photoabsorption and photoionization of trace elements. III. Isoelectronic sequences with electron number $19 \leq N \leq 26$. *Astron. Astrophys.* **2018**, *616*, A62. [CrossRef]
30. Kallman, T.R.; Bautista, M.A.; Goriely, S.; Mendoza, C.; Miller, J.M.; Palmeri, P.; Quinet, P.; Raymond, J. Spectrum Synthesis Modeling of the X-ray Spectrum of GRO J1655-40 Taken During the 2005 Outburst. *Astrophys. J.* **2009**, *701*, 865–884. [CrossRef]
31. García, J.; Ramírez, J.M.; Kallman, T.R.; Witthoeft, M.; Bautista, M.A.; Mendoza, C.; Palmeri, P.; Quinet, P. Modeling the Oxygen K Absorption in the Interstellar Medium: An XMM-Newton View of Sco X-1. *Astrophys. J.* **2011**, *731*, L15. [CrossRef]
32. Gatuzz, E.; García, J.; Mendoza, C.; Kallman, T.R.; Witthoeft, M.; Lohfink, A.; Bautista, M.A.; Palmeri, P.; Quinet, P. Photoionization Modeling of Oxygen K Absorption in the Interstellar Medium: The Chandra Grating Spectra of XTE J1817-330. *Astrophys. J.* **2013**, *768*, 60. [CrossRef]
33. Gatuzz, E.; García, J.; Mendoza, C.; Kallman, T.R.; Witthoeft, M.; Lohfink, A.; Bautista, M.A.; Palmeri, P.; Quinet, P. Erratum: "Photoionization Modeling of Oxygen K Absorption in the Interstellar Medium, the Chandra Grating Spectra of XTE J1817-330" (2013, ApJ, 768, 60). *Astrophys. J.* **2013**, *778*, 83. [CrossRef]

34. Gatuzz, E.; García, J.; Mendoza, C.; Kallman, T.R.; Bautista, M.A.; Gorczyca, T.W. Physical Properties of the Interstellar Medium Using High-resolution Chandra Spectra: O K-edge Absorption. *Astrophys J.* **2014**, *790*, 131. [CrossRef]
35. Gatuzz, E.; García, J.; Kallman, T.R.; Mendoza, C.; Gorczyca, T.W. ISMabs: A Comprehensive X-ray Absorption Model for the Interstellar Medium. *Astrophys. J.* **2015**, *800*, 29. [CrossRef]
36. Gatuzz, E.; García, J.A.; Kallman, T.R.; Mendoza, C. Oxygen, neon, and iron X-ray absorption in the local interstellar medium. *Astron. Astrophys.* **2016**, *588*, A111. [CrossRef]
37. Gatuzz, E.; Ness, J.U.; Gorczyca, T.W.; Hasoglu, M.F.; Kallman, T.R.; García, J.A. Carbon X-ray absorption in the local ISM: Fingerprints in X-ray Novae spectra. *Mon. Not. R. Astron. Soc.* **2018**, *479*, 2457–2463. [CrossRef]
38. Gatuzz, E.; García, J.A.; Kallman, T.R. On the discrepancy between the X-ray and UV absorption measurements of O VI in the local ISM. *Mon. Not. R. Astron. Soc.* **2019**, *483*, L75–L79. [CrossRef]
39. Gatuzz, E.; Gorczyca, T.W.; Hasoglu, M.F.; Schulz, N.S.; Corrales, L.; Mendoza, C. Silicon ISM X-ray absorption: the gaseous component. *Mon. Not. R. Astron. Soc.* **2020**, *498*, L20–L24. [CrossRef]
40. Deprince, J.; Palmeri, P.; Quinet, P.; Fritzsche, S.; Bautista, M.; Mendoza, C.; Kallman, T.R.; García, J.A. Plasma-Environment Effects on the Atomic Structure and K Lines of He- and Li-like Oxygen Ions. In *Workshop on Astrophysical Opacities*; Astronomical Society of the Pacific: San Francisco, CA, USA, 2018; ASP Conf. Ser. Volume 515, p. 289.
41. Deprince, J.; Bautista, M.A.; Fritzsche, S.; García, J.A.; Kallman, T.R.; Mendoza, C.; Palmeri, P.; Quinet, P. Plasma environment effects on K lines of astrophysical interest. I. Atomic structure, radiative rates, and Auger widths of oxygen ions. *Astron. Astrophys.* **2019**, *624*, A74. [CrossRef]
42. Deprince, J.; Bautista, M.A.; Fritzsche, S.; García, J.A.; Kallman, T.; Mendoza, C.; Palmeri, P.; Quinet, P. Plasma environment effects on K lines of astrophysical interest. II. Ionization potentials, K thresholds, radiative rates, and Auger widths in Ne- through He-like iron ions (Fe XVII–Fe XXV). *Astron. Astrophys.* **2019**, *626*, A83. [CrossRef]
43. Deprince, J.; Bautista, M.A.; Fritzsche, S.; García, J.A.; Kallman, T.R.; Mendoza, C.; Palmeri, P.; Quinet, P. Plasma-environment effects on K lines of astrophysical interest. III. IPs, K thresholds, radiative rates, and Auger widths in Fe IX–Fe XVI. *Astron. Astrophys.* **2020**, *635*, A70. [CrossRef]
44. Deprince, J.; Bautista, M.; Fritzsche, S.; García, J.; Kallman, T.; Mendoza, C.; Palmeri, P.; Quinet, P. K-line X-ray fluorescence from highly charged iron ions under dense astrophysical plasma conditions. *X-ray Spectrom.* **2020**, *49*, 29–32. [CrossRef]
45. Deprince, J.; Bautista, M.A.; Fritzsche, S.; García, J.A.; Kallman, T.R.; Mendoza, C.; Palmeri, P.; Quinet, P. Plasma environment effects on K lines of astrophysical interest. IV. IPs, K thresholds, radiative rates, and Auger widths in Fe II-Fe VIII. *Astron. Astrophys.* **2020**, *643*, A57. [CrossRef]
46. Kallman, T.; Bautista, M.; Deprince, J.; Garcia, J.A.; Mendoza, C.; Ogorzalek, A.; Palmeri, P.; Quinet, P. Photoionization Models for High Density Gas. *arXiv* **2020**, arXiv:2011.10603.
47. Hitomi Collaboration; Aharonian, F.; Akamatsu, H.; Akimoto, F.; Allen, S.W.; Anabuki, N.; Angelini, L.; Arnaud, K.; Audard, M.; Awaki, H.; et al. The quiescent intracluster medium in the core of the Perseus cluster. *Nature* **2016**, *535*, 117–121. [CrossRef]
48. Nikolić, D.; Gorczyca, T.W.; Korista, K.T.; Ferland , G.J.; Badnell, N.R. Suppression of Dielectronic Recombination due to Finite Density Effects. *Astrophys. J.* **2013**, *768*, 82. [CrossRef]
49. Nikolić, D.; Gorczyca, T.W.; Korista, K.T.; Chatzikos, M.; Ferland, G.J.; Guzmán, F.; van Hoof, P.A.M.; Williams, R.J.R.; Badnell, N.R. Suppression of Dielectronic Recombination Due to Finite Density Effects. II. Analytical Refinement and Application to Density-dependent Ionization Balances and AGN Broad-line Emission. *Astrophys. J. Suppl.* **2018**, *237*, 41. [CrossRef]
50. García, J.A.; Fabian, A.C.; Kallman, T.R.; Dauser, T.; Parker, M.L.; McClintock, J.E.; Steiner, J.F.; Wilms, J. The effects of high density on the X-ray spectrum reflected from accretion discs around black holes. *Mon. Not. R. Astron. Soc.* **2016**, *462*, 751–760. [CrossRef]
51. García, J.A.; Kallman, T.R.; Bautista, M.; Mendoza, C.; Deprince, J.; Palmeri, P.; Quinet, P. The Problem of the High Iron Abundance in Accretion Disks around Black Holes. In *Workshop on Astrophysical Opacities*; Astronomical Society of the Pacific: San Francisco, CA, USA, 2018; ASP Conf. Ser. Volume 515; p. 282.
52. Leutenegger, M.A.; Kühn, S.; Micke, P.; Steinbrügge, R.; Stierhof, J.; Shah, C.; Hell, N.; Bissinger, M.; Hirsch, M.; Ballhausen, R.; et al. High-Precision Determination of Oxygen K_α Transition Energy Excludes Incongruent Motion of Interstellar Oxygen. *Phys. Rev. Lett.* **2020**, *125*, 243001. [CrossRef] [PubMed]
53. Greisen, E.W. FITS: A Remarkable Achievement in Information Exchange. In *Information Handling in Astronomy—Historical Vistas*; Heck, A., Ed.; Kluwer Academic Publishers: Dordrecht, The Netherlands, 2003; Astrophysics and Space Science Library Volume 285; p. 71. [CrossRef]
54. Pence, W.D.; Chiappetti, L.; Page, C.G.; Shaw, R.A.; Stobie, E. Definition of the Flexible Image Transport System (FITS), version 3.0. *Astron. Astrophys.* **2010**, *524*, A42. [CrossRef]
55. Cowan, R.D. *The Theory of Atomic Structure and Spectra*; University of California Press: Berkeley, CA, USA, 1981.
56. Berrington, K.A.; Eissner, W.B.; Norrington, P.H. RMATRX1: Belfast atomic R-matrix codes. *Comput. Phys. Commun.* **1995**, *92*, 290–420. [CrossRef]
57. Burke, P.G. *R-Matrix Theory of Atomic Collisions*; Springer: New York, NY, USA, 2011.
58. Gorczyca, T.W.; Robicheaux, F. Auger decay of the photoexcited $2p^{-1}nl$ Rydberg series in argon. *Phys. Rev. A* **1999**, *60*, 1216–1225. [CrossRef]

59. Kramida, A.; Yu. Ralchenko.; Reader, J.; NIST ASD Team. *NIST Atomic Spectra Database*; National Institute of Standards and Technology: Gaithersburg, MD, USA, 2020. Available online: https://physics.nist.gov/asd (accessed on 15 November 2020).
60. Cunto, W.; Mendoza, C.; Ochsenbein, F.; Zeippen, C.J. TOPbase at the CDS. *Astron. Astrophys.* **1993**, *275*, L5–L8.
61. Dere, K.P.; Landi, E.; Mason, H.E.; Monsignori Fossi, B.C.; Young, P.R. CHIANTI—An atomic database for emission lines. *Astron. Astrophys. Suppl. Ser.* **1997**, *125*, 149–173. [CrossRef]
62. Hummer, D.G.; Berrington, K.A.; Eissner, W.; Pradhan, A.K.; Saraph, H.E.; Tully, J.A. Atomic data from the IRON project. I. Goals and methods. *Astron. Astrophys.* **1993**, *279*, 298–309.
63. Pradhan, A.K.; Peng, J. Atomic Data For The Analysis of Emission Lines. In *The Analysis of Emission Lines*; Williams, R.E.W., Livio, M., Eds.; Space Institute Symposium Series; Cambridge University Press: Cambridge, UK, 1995; Volume 8, pp. 8–34.
64. Badnell, N.R.; O'Mullane, M.G.; Summers, H.P.; Altun, Z.; Bautista, M.A.; Colgan, J.; Gorczyca, T.W.; Mitnik, D.M.; Pindzola, M.S.; Zatsarinny, O. Dielectronic recombination data for dynamic finite-density plasmas. I. Goals and methodology. *Astron. Astrophys.* **2003**, *406*, 1151–1165. [CrossRef]
65. Badnell, N.R. Radiative Recombination Data for Modeling Dynamic Finite-Density Plasmas. *Astrophys. J. Suppl. Ser.* **2006**, *167*, 334–342. [CrossRef]
66. Eissner, W.; Jones, M.; Nussbaumer, H. Techniques for the calculation of atomic structures and radiative data including relativistic corrections. *Comput. Phys. Commun.* **1974**, *8*, 270–306. [CrossRef]
67. Badnell, N.R. A Breit-Pauli distorted wave implementation for AUTOSTRUCTURE. *Comput. Phys. Commun.* **2011**, *182*, 1528–1535. [CrossRef]
68. Parpia, F.A.; Fischer, C.F.; Grant, I.P. GRASP92: A package for large-scale relativistic atomic structure calculations. *Comput. Phys. Commun.* **1996**, *94*, 249–271. [CrossRef]
69. Hickman, A.P. Complex potential model for dielectronic recombination. *J. Phys. B At. Mol. Phys.* **1984**, *17*, L101–L106. [CrossRef]
70. Robicheaux, F.; Gorczyca, T.W.; Pindzola, M.S.; Badnell, N.R. Inclusion of radiation damping in the close-coupling equations for electron-atom scattering. *Phys. Rev. A* **1995**, *52*, 1319–1333. [CrossRef] [PubMed]
71. Davies, P.C.W.; Seaton, M.J. Radiation damping in the optical continuum. *J. Phys. B At. Mol. Phys.* **1969**, *2*, 757–765. [CrossRef]
72. Bell, R.H.; Seaton, M.J. Dielectronic recombination. I. General theory. *J. Phys. B At. Mol. Phys.* **1985**, *18*, 1589–1629. [CrossRef]
73. Froese Fischer, C. *The Hartree-Fock Method for Atom*; Wiley: New York, NY, USA, 1977.
74. Froese Fischer, C. A general multi-configuration Hartree-Fock program. *Comput. Phys. Commun.* **1991**, *64*, 431–454. [CrossRef]
75. Froese Fischer, C.; Brage, T.; Jönsson, P. *Computational Atomic Structure: An MCHF Approach*; Institute of Physics Publ.: Bristol, UK, 1997.
76. Stolte, W.C.; Lu, Y.; Samson, J.A.R.; Hemmers, O.; Hansen, D.L.; Whitfield, S.B.; Wang, H.; Glans, P.; Lindle, D.W. The K-shell Auger decay of atomic oxygen. *J. Phys. B At. Mol. Phys.* **1997**, *30*, 4489–4497. [CrossRef]
77. Liao, J.Y.; Zhang, S.N.; Yao, Y. Wavelength Measurements of K Transitions of Oxygen, Neon, and Magnesium with X-ray Absorption Lines. *Astrophys. J.* **2013**, *774*, 116. [CrossRef]
78. Juett, A.M.; Schulz, N.S.; Chakrabarty, D. High-Resolution X-ray Spectroscopy of the Interstellar Medium: Structure at the Oxygen Absorption Edge. *Astrophys. J.* **2004**, *612*, 308–318. [CrossRef]
79. McLaughlin, B.M.; Ballance, C.P.; Bowen, K.P.; Gardenghi, D.J.; Stolte, W.C. High Precision K-shell Photoabsorption Cross Sections for Atomic Oxygen: Experiment and Theory. *Astrophys. J.* **2013**, *771*, L8. [CrossRef]
80. McLaughlin, B.M.; Ballance, C.P.; Bowen, K.P.; Gardenghi, D.J.; Stolte, W.C. Erratum: "High Precision K-Shell Photoabsorption Cross Sections for Atomic Oxygen: Experiment and Theory" (2013, ApJL, 771, l8). *Astrophys. J.* **2013**, *779*, L31. [CrossRef]
81. Menzel, A.; Benzaid, S.; Krause, M.O.; Caldwell, C.D.; Hergenhahn, U.; Bissen, M. Natural widths in open-shell atoms: The K absorption spectrum of atomic oxygen. *Phys. Rev. A* **1996**, *54*, R991–R994. [CrossRef]
82. Caldwell, C.; Schaphorst, S.; Krause, M.; Jiménez-Mier, J. Photoexcited K Auger spectra of atomic and molecular oxygen. *JESRP* **1994**, *67*, 243–259. [CrossRef]
83. Fabian, A.C.; Ross, R.R. X-ray Reflection. *Space Sci. Rev.* **2010**, *157*, 167–176. [CrossRef]
84. Badnell, N.R.; Pindzola, M.S.; Dickson, W.J.; Summers, H.P.; Griffin, D.C.; Lang, J. Electric Field Effects on Dielectronic Recombination in a Collisional-Radiative Model. *Astrophys. J.* **1993**, *407*, L91. [CrossRef]
85. Nahar, S.N.; Pradhan, A.K. Electron-ion recombination in the close-coupling approximation. *Phys. Rev. Lett.* **1992**, *68*, 1488–1491. [CrossRef] [PubMed]
86. Nahar, S.N.; Pradhan, A.K. Unified treatment of electron-ion recombination in the close-coupling approximation. *Phys. Rev A* **1994**, *49*, 1816–1835. [CrossRef] [PubMed]
87. García, J.; Kallman, T.R. X-ray Reflected Spectra from Accretion Disk Models. I. Constant Density Atmospheres. *Astrophys. J.* **2010**, *718*, 695–706. [CrossRef]
88. García, J.; Dauser, T.; Reynolds, C.S.; Kallman, T.R.; McClintock, J.E.; Wilms, J.; Eikmann, W. X-ray Reflected Spectra from Accretion Disk Models. III. A Complete Grid of Ionized Reflection Calculations. *Astrophys. J.* **2013**, *768*, 146. [CrossRef]
89. Aldrovandi, S.M.V.; Pequignot, D. Radiative and Dielectronic Recombination Coefficients for Complex Ions. *Astron. Astrophys.* **1973**, *25*, 137.
90. Bautista, M.A.; Pradhan, A.K. Ionization Structure and Spectra of Iron in Gaseous Nebulae. *Astrophys. J.* **1998**, *492*, 650–676. [CrossRef]

91. Bautista, M.A. Theoretical Calculations of Atomic Data for Spectroscopy. In *Atomic Data Needs for X-ray Astronomy*; Bautista, M.A., Kallman, T.R., Pradhan, A.K., Eds.; NASA/CP-2000-209968; NASA Goddard Space Flight Center: Greenbelt, MD, USA, 2000; pp. 25–40.
92. Ralchenko, Y.; Kramida, A. Development of NIST Atomic Databases and Online Tools. *Atoms* **2020**, *8*, 56. [CrossRef]
93. Albert, D.; Antony, B.K.; Ba, Y.A.; Babikov, Y.L.; Bollard, P.; Boudon, V.; Delahaye, F.; Del Zanna, G.; Dimitrijević, M.S.; Drouin, B.J.; et al. A Decade with VAMDC: Results and Ambitions. *Atoms* **2020**, *8*, 76. [CrossRef]
94. Mendoza, C.; Boswell, J.; Ajoku, D.; Bautista, M. AtomPy: An Open Atomic Data Curation Environment for Astrophysical Applications. *Atoms* **2014**, *2*, 123–156. [CrossRef]
95. Juan de Dios, L.; Rodríguez, M. The impact of atomic data selection on nebular abundance determinations. *Mon. Not. R. Astron. Soc.* **2017**, *469*, 1036–1053. [CrossRef]
96. Morisset, C.; Luridiana, V.; García-Rojas, J.; Gómez-Llanos, V.; Bautista, M. Atomic Data Assessment with PyNeb. *Atoms* **2020**, *8*, 66. [CrossRef]
97. Aldrovandi, S.M.V.; Pequignot, D. Erratum; Radiative and Dielectronic Recombination Coefficients for Complex Ions. *Astron. Astrophys.* **1976**, *47*, 321.
98. Kingdon, J.B.; Ferland, G.J. Rate Coefficients for Charge Transfer between Hydrogen and the First 30 Elements. *Astrophys. J. Suppl. Ser.* **1996**, *106*, 205. [CrossRef]
99. Nussbaumer, H.; Storey, P.J. Dielectronic recombination at low temperatures. III—Recombination coefficients for Mg, Al, Si. *Astron. Astrophys. Suppl. Ser.* **1986**, *64*, 545–555.
100. Gould, R.J.; Thakur, R.K. Atomic processes in a low-density hydrogen-helium plasma. *Ann. Phys.* **1970**, *61*, 351–386. [CrossRef]
101. Burgess, A.; Tully, J.A. On the analysis of collision strengths and rate coefficients. *Astron. Astrophys.* **1992**, *254*, 436–453.
102. Verner, D.A.; Yakovlev, D.G. Analytic FITS for partial photoionization cross sections. *Astron. Astrophys. Suppl. Ser.* **1995**, *109*, 125–133.
103. Callaway, J. Effective Collision Strengths for Hydrogen and Hydrogen-Like Ions. *At. Data Nucl. Data Tables* **1994**, *57*, 9–20. [CrossRef]
104. Kato, T.; Nakazaki, S. Recommended Data for Excitation Rate Coefficients of Helium Atoms and Helium-like Ions by Electron Impact. *Atom. Data Nucl. Data Tables* **1989**, *42*, 313. [CrossRef]
105. Keenan, F.P.; McCann, S.M.; Kingston, A.E. Electron Impact Excitation Rates for Transitions from the Ground State to the n = 2 and 3 levels in Helium-Like Ions. *Phys. Scr.* **1987**, *35*, 432–436. [CrossRef]
106. Zhang, H.; Sampson, D.H. Collision Rates for Excitation of Helium-like Ions with Inclusion of Resonance Effects. *Astrophys. J. Suppl. Ser.* **1987**, *63*, 487. [CrossRef]
107. Sampson, D.H.; Goett, S.J.; Clark, R.E.H. Electron-Impact Collision Strengths for Inner-Shell Excitation of Doubly Excited Levels from Singly Excited Levels in He-like Ions. *At. Data Nucl. Data Tables* **1983**, *28*, 299. [CrossRef]
108. Bhatia, A.K.; Fawcett, B.C.; Phillips, K.J.H.; Lemen, J.R.; Mason, H.E. A comparison of theoretical and solar-flare intensity ratios for the Fe XIX X-ray lines. *Mon. Not. R. Astron. Soc.* **1989**, *240*, 421–444. [CrossRef]
109. Gu, M.F.; Holczer, T.; Behar, E.; Kahn, S.M. Inner-Shell Absorption Lines of Fe VI-Fe XVI: A Many-Body Perturbation Theory Approach. *Astrophys. J.* **2006**, *641*, 1227–1232. [CrossRef]
110. Foster, A.R.; Ji, L.; Smith, R.K.; Brickhouse, N.S. Updated Atomic Data and Calculations for X-ray Spectroscopy. *Astrophys. J.* **2012**, *756*, 128. [CrossRef]
111. Bryans, P.; Badnell, N.R.; Gorczyca, T.W.; Laming, J.M.; Mitthumsiri, W.; Savin, D.W. Collisional Ionization Equilibrium for Optically Thin Plasmas. I. Updated Recombination Rate Coefficients for Bare through Sodium-like Ions. *Astrophys. J. Suppl. Ser.* **2006**, *167*, 343–356. [CrossRef]
112. Abu-Salbi, N.; Callaway, J. Electron-impact excitation of hydrogenic ions. *Phys. Rev. A* **1981**, *24*, 2372–2386. [CrossRef]
113. Aggarwal, K.M.; Callaway, J.; Kingston, A.E.; Unnikrishnan, K. Excitation Rate Coefficients for Transitions among the N = 1, 2, and 3 Levels of He+. *Astrophys. J. Suppl. Ser.* **1992**, *80*, 473. [CrossRef]
114. Aggarwal, K.M.; Kingston, A.E. Electron impact excitation of C VI: Collision strengths and rate coefficients. *J. Phys. B At. Mol. Phys.* **1991**, *24*, 4583–4602. [CrossRef]
115. Aggarwal, K.M.; Kingston, A.E. Electron impact excitation of Ne X: Collision strengths and rate coefficients. *Phys. Scr.* **1991**, *44*, 517–527. [CrossRef]
116. Aggarwal, K.M.; Kingston, A.E. Electron impact excitation of Si XIV: Collision strengths and rate coefficients. *Phys. Scr.* **1992**, *46*, 193–201. [CrossRef]
117. Aggarwal, K.M.; Kingston, A.E. Electron impact excitation of Ca XX: Collision strengths and rate coefficients. *J. Phys. B At. Mol. Phys.* **1992**, *25*, 751–771. [CrossRef]
118. Aggarwal, K.M.; Kingston, A.E. Electron Impact Excitation of Fe xxvi: Collision Strengths and Rate Coefficients. *Astrophys J. Suppl.* **1993**, *85*, 187. [CrossRef]
119. Binello, A.M.; Mason, H.E.; Storey, P.J. Atomic data from the IRON Project. XXV. Electron impact excitation of fine-structure transitions in the ground configuration of Fe XII. *Astron. Astrophys. Suppl. Ser.* **1998**, *127*, 545–553. [CrossRef]
120. Flower, D.R. Excitation of the Fe XII spectrum in the solar corona. *Astron. Astrophys.* **1977**, *54*, 163–166.
121. Tayal, S.S.; Henry, R.J.W.; Pradhan, A.K. Electron Excitation of Fine-Structure Transitions within the Ground $3s^2 3p^3$ Configuration in Fe XII. *Astrophys. J.* **1987**, *319*, 951. [CrossRef]

122. Berrington, K.A.; Nakazaki, S.; Norrington, P.H. Atomic data from the IRON Project. XLI. Electron excitation rates among the $3d^2$ fine-structure levels of Ca-like Fe VII. *Astron. Astrophys. Suppl. Ser.* **2000**, *142*, 313–316. [CrossRef]
123. Keenan, F.P.; Norrington, P.H. Relative emission line strengths for Fe VII in astrophysical plasmas. *Astron. Astrophys.* **1987**, *181*, 370–372.
124. Gau, J.N.; Henry, R.J.W. Excitation of lithiumlike ions by electron impact. *Phys. Rev. A* **1977**, *16*, 986–990. [CrossRef]
125. Wiese, W.L.; Smith, M.W.; Glennon, B.M. *Atomic Transition Probabilities. Vol.: Hydrogen through Neon. A Critical Data Compilation*; US Government Printing Office: Washington, DC, USA, 1966.
126. Martin, I.; Karwowski, J.; Diercksen, G.H.F.; Barrientos, C. Transition probabilities in the lithium sequence. *Astron. Astrophys. Suppl. Ser.* **1993**, *100*, 595–605.
127. Zhang, H.L.; Sampson, D.H.; Fontes, C.J. Relativistic Distorted-Wave Collision Strengths for the 85 Li-like Ions with 8 <= Z <= 92. *At. Data Nucl. Data Tables* **1990**, *44*, 31. [CrossRef]
128. Berrington, K.A.; Burke, P.G.; Dufton, P.L.; Kingston, A.E. Electron-Impact-Excitation Collision Strengths for Be-like Ions. II. Intermediate-Energy Region and Collision Rates. *At. Data Nucl. Data Tables* **1985**, *33*, 195. [CrossRef]
129. Berrington, K.A.; Burke, V.M.; Burke, P.G.; Scialla, S. Electron impact excitation of n = 3 states of C III: An application of a new R-matrix package. *J. Phys. B At. Mol. Phys.* **1989**, *22*, 665–676. [CrossRef]
130. Muehlethaler, H.P.; Nussbaumer, H. Transition probabilities within $2s^2$-2s2p-$2p^2$ in the Be I sequence, Be I—Ni XXV. *Astron. Astrophys.* **1976**, *48*, 109–114.
131. Sampson, D.H.; Goett, S.J.; Clark, R.E.H. Collision Strengths and Line Strengths for Fine-Structure Transitions between the $2l_a2l_b$ Configurations and the $2l'_a3l'_b$ Configurations in Be-like Ions. *At. Data Nucl. Data Tables* **1984**, *30*, 125. [CrossRef]
132. Zhang, H.L.; Sampson, D.H. Relativistic Distorted-Wave Collision Strengths and Oscillator Strengths for the 45 Δn =0 Transitions with n = 2 in the 85 Be-like Ions with 8 <= Z <= 92. *At. Data Nucl. Data Tables* **1992**, *52*, 143. [CrossRef]
133. Ramsbottom, C.A.; Berrington, K.A.; Hibbert, A.; Bell, K.L. Electron impact excitation rates for transitions involving the n = 2 and n = 3 levels of beryllium-like N IV. *Phys. Scr.* **1994**, *50*, 246–253. [CrossRef]
134. Kato, T.; Lang, J.; Berrington, K.A. Intensity Ratios of Emission Lines for O V Ions for Temperature and Density Diagnostics, and Recommended Excitation Rate Coefficients. *At. Data Nucl. Data Tables* **1990**, *44*, 133. [CrossRef]
135. Dankwort, W.; Trefftz, E. Breit-Pauli approximation for highly ionized boron-like ions, up to Fe XXII. *Astron. Astrophys.* **1978**, *65*, 93–98.
136. Nussbaumer, H.; Storey, P.J. C II two-electron transitions. *Astron. Astrophys.* **1981**, *96*, 91–95.
137. Lennon, D.J.; Dufton, P.L.; Hibbert, A.; Kingston, A.E. C II emission lines formed in optically thin plasmas. *Astrophys. J.* **1985**, *294*, 200–206. [CrossRef]
138. Blum, R.D.; Pradhan, A.K. Rate Coefficients for the Excitation of Infrared and Ultraviolet Lines in C II, N III, and O IV. *Astrophys. J. Suppl. Ser.* **1992**, *80*, 425. [CrossRef]
139. Nussbaumer, H.; Storey, P.J. N III lines for solar diagnostics. *Astron. Astrophys.* **1979**, *71*, L5–L8.
140. Stafford, R.P.; Hibbert, A.; Bell, K.L. Accurate transition probabilities for spectral lines of N III. *Mon. Not. R. Astron. Soc.* **1993**, *260*, L11–L14. [CrossRef]
141. Stafford, R.P.; Bell, K.L.; Hibbert, A. Electron impact excitation of N III—Fine-structure collision strengths and Maxwellian-averaged rate coefficients. *Mon. Not. R. Astron. Soc.* **1994**, *266*, 715. [CrossRef]
142. Stafford, R.P.; Bell, K.L.; Hibbert, A.; Wijesundera, W.P. Electron Impact Excitation of NII—Fine Structure Collision Strengths and Maxwellian-Averaged Rate Coefficients. *Mon. Not. R. Astron. Soc.* **1994**, *268*, 816. [CrossRef]
143. Bhatia, A.K.; Feldman, U.; Seely, J.F. Atomic Data and Spectral Line Intensities for the Boron Isoelectronic Sequence (Ar XIV through Kr XXXII). *At. Data Nucl. Data Tables* **1986**, *35*, 319. [CrossRef]
144. Zhang, H.L.; Graziani, M.; Pradhan, A.K. Atomic Data from the Iron Project: III. Rate Coefficients for Electron Impact Excitation of Boron-like Ions: NE VI, MG VIII, AL IX, SI X, S XII, AR XIV, CA XVI and Fe XXII. *Astron. Astrophys.* **1994**, *283*, 319.
145. Sampson, D.H.; Weaver, G.M.; Goett, S.J.; Zhang, H.; Clark, R.E.H. Collision Strengths and Line Strengths for All Transitions among the Levels of the $1s^22s^22p$, $1s^22s2p^2$, and $1s^22p^3$, Configurations of Boron-like Ions. *At. Data Nucl. Data Tables* **1986**, *35*, 223. [CrossRef]
146. Bell, K.L.; Hibbert, A.; Stafford, R.P. Transition probabilities for some spectral lines of singly ionised nitrogen. *Phys. Scr.* **1995**, *52*, 240–251. [CrossRef]
147. Aggarwal, K.M. Electron excitation rates among fine structure levels in O III. *Astrophys. J. Suppl. Ser.* **1983**, *52*, 387–398. [CrossRef]
148. Aggarwal, K.M. Line intensity ratios for transitions in O III. *Astron. Astrophys.* **1985**, *146*, 149–158.
149. Bhatia, A.K.; Kastner, S.O. Collision Strengths and Transition Rates for O III. *At. Data Nucl. Data Tables* **1993**, *54*, 133–164. [CrossRef]
150. Lennon, D.J.; Burke, V.M. Atomic data from the IRON project. II. Effective collision strengths for infrared transitions in carbon-like ions. *Astron. Astrophys. Suppl. Ser.* **1994**, *103*, 273–277.
151. Aggarwal, K.M. Electron impact excitation rates for fine-structure transitions in NE V and SI IX—An R-matrix approach. *Astrophys. J. Suppl. Ser.* **1984**, *54*, 1–15. [CrossRef]
152. Bhatia, A.K.; Doschek, G.A. Atomic Data and Spectral Line Intensities for C-like Ne V. *At. Data Nucl. Data Tables* **1993**, *55*, 315–348. [CrossRef]

153. Bhatia, A.K.; Doschek, G.A. Atomic Data and Spectral Line Intensities for C-Like Si IX. *At. Data Nucl. Data Tables* **1993**, *55*, 281–314. [CrossRef]
154. Bhatia, A.K.; Doschek, G.A. Atomic Data and Spectral Line Intensities for C-like Mg VII. *At. Data Nucl. Data Tables* **1995**, *60*, 145. [CrossRef]
155. Bhatia, A.K.; Kastner, S.O. Atomic parameters for carbon-like S XI. *J. Quant. Spectros. Radiat. Transf.* **1987**, *37*, 527–529. [CrossRef]
156. Dere, K.P.; Mason, H.E.; Widing, K.G.; Bhatia, A.K. XUV electron density diagnostics for solar flares. *Astrophys. J. Suppl. Ser.* **1979**, *40*, 341–364. [CrossRef]
157. Mason, H.E.; Bhatia, A.K. Theoretical intensity ratios for the UV lines of Mg VII, Si IX and S XI. *Mon. Not. R. Astron. Soc.* **1978**, *184*, 423–437. [CrossRef]
158. Froese Fischer, C.; Saha, H.P. Multiconfiguration Hartree-Fock Results with Breit-Pauli Corrections for Transitions in the Carbon Sequence. *Phys. Scr.* **1985**, *32*, 181–194. [CrossRef]
159. Aggarwal, K.M.; Berrington, K.A.; Keenan, F.P. Effective Collision Strengths among Fine-Structure Levels of CA XV. *Astrophys. J. Suppl. Ser.* **1990**, *72*, 815. [CrossRef]
160. Aggarwal, K.M.; Berrington, K.A.; Keenan, F.P. Effective collision strengths among fine-structure levels of CA XV: Erratum. *Astrophys. J. Suppl. Ser.* **1991**, *77*, 441–449. [CrossRef]
161. Bhatia, A.K.; Mason, H.E. Theoretical atomic structure and electron scattering data for ions in the nitrogen isoelectronic sequence—MG VI, SI VIII, S X, A XII and CA XIV. *Mon. Not. R. Astron. Soc.* **1980**, *190*, 925–929. [CrossRef]
162. Bhatia, A.K.; Seely, J.F.; Feldman, U. Atomic Data and Spectral Line Intensities for the Nitrogen Isoelectronic Sequence (Ar XII through Kr XXX). *At. Data Nucl. Data Tables* **1989**, *43*, 99. [CrossRef]
163. Mason, H.E.; Bhatia, A.K.; Doschek, G.A.; Feldman, U. Fe XXI as an electron density diagnostic in solar flares. *Astron. Astrophys.* **1979**, *73*, 74–81.
164. Aggarwal, K.M. Collision Strengths and Excitation Rate Coefficients for Transitions in Fe XXI. *Astrophys. J. Suppl. Ser.* **1991**, *77*, 677. [CrossRef]
165. Bhatia, A.K.; Feldman, U.; Doschek, G.A. New atomic data for Si/6+/, S/8+/ and Ar/10+/. *Astron. Astrophys.* **1979**, *80*, 22–26.
166. McLaughlin, B.M.; Bell, K.L. Analytical FITS for Electron Collisionally Excited Effective Collision Strengths of O II. *Astrophys. J. Suppl. Ser.* **1994**, *94*, 825. [CrossRef]
167. Loulergue, M.; Mason, H.E.; Nussbaumer, H.; Storey, P.J. Fe XIX transitions within the N = 2 complex. *Astron. Astrophys.* **1985**, *150*, 246–250.
168. Blackford, H.M.S.; Hibbert, A. Transitions in Fluorine-Like Ions. *At. Data Nucl. Data Tables* **1994**, *58*, 101–164. [CrossRef]
169. Butler, K.; Zeippen, C.J. Atomic data from the IRON Project. V. Effective collision strengths for transitions in the ground configuration of oxygen-like ions. *Astron. Astrophys. Suppl. Ser.* **1994**, *108*, 1–8.
170. Sampson, D.H.; Zhang, H.L.; Fontes, C.J. Relativistic Distorted-Wave Collision Strengths and Oscillator Strengths for F-like Ions with 22 <= Z <= 92. *At. Data Nucl. Data Tables* **1991**, *48*, 25. [CrossRef]
171. Cornille, M.; Dubau, J.; Loulergue, M.; Bely-Dubau, F.; Faucher, P. Theoretical analysis of the Fe XVIII X-ray spectrum and application to solar coronal observations. *Astron. Astrophys.* **1992**, *259*, 669–681.
172. Bhatia, A.K.; Feldman, U.; Seely, J.F. Atomic Data and Spectral Line Intensities for the Neon Isoelectronic Sequence (Si V through Kr XXVII). *At. Data Nucl. Data Tables* **1985**, *32*, 435. [CrossRef]
173. Hibbert, A.; Ledourneuf, M.; Mohan, M. Energies, Oscillator Strengths, and Lifetimes for Neon-like Ions Up to Kr XXVII. *At. Data Nucl. Data Tables* **1993**, *53*, 23–112. [CrossRef]
174. Saraph, H.E.; Tully, J.A. Atomic data from the IRON project. IV. Electron excitation of the $^2P^\circ_{3/2}$–$^2P^\circ_{1/2}$ fine structure transition in fluorine-like ions. *Astron. Astrophys. Suppl. Ser.* **1994**, *107*, 29–38.
175. Mohan, M.; Baluja, K.L.; Hibbert, A. Electron-impact excitation of MG IV using the R-matrix method. *Phys. Scr.* **1988**, *38*, 699–701. [CrossRef]
176. Zhang, H.; Sampson, D.H.; Clark, R.E.H.; Mann, J.B. Collision Strengths and Oscillator Strengths for Excitation to the n = 3 and 4 Levels of Neon-like Ions. *At. Data Nucl. Data Tables* **1987**, *37*, 17. [CrossRef]
177. Bhatia, A.K.; Doschek, G.A. Atomic Data and Spectral Line Intensities for Ne-like Fe XVII. *At. Data Nucl. Data Tables* **1992**, *52*, 1. [CrossRef]
178. Mohan, M.; Le Dourneuf, M. Electron-impact excitation from the Si(5+) ground state, using the R-matrix method. *Astron. Astrophys.* **1990**, *227*, 285–288.
179. Mohan, M.; Hibbert, A.; Baluja, K.L. Electron impact excitation of S VIII from its ground state. *J. Phys. B At. Mol. Phys.* **1987**, *20*, 2565–2570. [CrossRef]
180. Sampson, D.H.; Zhang, H.L.; Fontes, C.J. Relativistic Distorted-Wave Collision Strengths and Oscillator Strengths for the 71 Na-like Ions with 22 <= Z <= 92. *At. Data Nucl. Data Tables* **1990**, *44*, 209. [CrossRef]
181. Dufton, P.L.; Hibbert, A.; Kingston, A.E.; Doschek, G.A. Si III line ratios in the Sun. *Astrophys. J.* **1983**, *274*, 420–428. [CrossRef]
182. Mason, H.E. The excitation of several iron and calcium lines in the visible spectrum of the solar corona. *Mon. Not. R. Astron. Soc.* **1975**, *170*, 651–689. [CrossRef]
183. Christensen, R.B.; Norcross, D.W.; Pradhan, A.K. Electron-impact excitation of ions in the magnesium sequence. II. S v, Ar vii, Ca ix, Cr xiii, and Ni xvii. *Phys. Rev. A* **1986**, *34*, 4704–4715. [CrossRef]
184. Lanzafame, A.C. Si II resonance multiplets in the Sun. *Astron. Astrophys.* **1994**, *287*, 972–981.

185. Mohan, M.; Hibbert, A.; Berrington, K.A.; Burke, P.G. Electron impact excitation of neon-like S VII from its ground state. *J. Phys. B At. Mol. Phys.* **1990**, *23*, 989–996. [CrossRef]
186. Bhatia, A.K.; Doschek, G.A.; Feldman, U. Atomic data for S IV and solar observations of the $3s^2 3p^2 P$–$3s3p^2\ ^4P$ multiplet. *Astron. Astrophys.* **1980**, *86*, 32–35.
187. Dufton, P.L.; Hibbert, A.; Kingston, A.E.; Doschek, G.A. S IV emission-line ratios in the sun. *Astrophys. J.* **1982**, *257*, 338–344. [CrossRef]
188. Fischer, C.F.; Liu, B. Energy Levels, Lifetimes, Wavelengths, and Transition Probabilities of Fe XIV. *At. Data Nucl. Data Tables* **1986**, *34*, 261. [CrossRef]
189. Czyzak, S.J.; Krueger, T.K. On the Excited Levels of Fe VIII. *Astrophys. J.* **1966**, *144*, 381. [CrossRef]
190. Fawcett, B.C. Computed Oscillator Strengths and Energy Levels for Potassium-like Ions V V, Cr VI, Mn VII, Fe VIII, Co IX, Ni X, and Cu XI with Calculated Wavelengths and Wavelengths Derived from Established Data. *At. Data Nucl. Data Tables* **1989**, *43*, 71. [CrossRef]
191. Dufton, P.L.; Kingston, A.E. Effective collision strengths for Si III. *Mon. Not. R. Astron. Soc.* **1989**, *241*, 209–214. [CrossRef]
192. Nussbaumer, H.; Storey, P.J.; Storey, P.J. Forbidden emission lines of Fe VII. *Astron. Astrophys.* **1982**, *113*, 21–26.
193. Dufton, P.L.; Kingston, A.E. Effective collision strengths for Si II. *Mon. Not. R. Astron. Soc.* **1991**, *248*, 827–828. [CrossRef]
194. Bhadra, K.; Henry, R.J.W. Oscillator strengths and collision strengths for S IV. *Astrophys. J.* **1980**, *240*, 368–373. [CrossRef]
195. Fawcett, B.C.; Mason, H.E. Collision Strengths and Oscillator Strengths for Fe IX. *At. Data Nucl. Data Tables* **1991**, *47*, 17. [CrossRef]
196. Mason, H.E. An Assessment of Theoretical Electron Excitation Data for Fe IX-Fe XIV. *At. Data Nucl. Data Tables* **1994**, *57*, 305–328. [CrossRef]
197. Pindzola, M.S.; Griffin, D.C.; Bottcher, C. Coupling effects for electron-impact excitation in the potassium isoelectronic sequence. *Phys. Rev. A* **1989**, *39*, 2385–2391. [CrossRef]
198. Fawcett, B.C.; Mason, H.E. A Slater Parameter Optimization Method Applied to the Computation of Collision Strengths for Fe XIII. *At. Data Nucl. Data Tables* **1989**, *43*, 245. [CrossRef]
199. Aggarwal, K.M.; Berrington, K.A.; Burke, P.G.; Kingston, A.E.; Pathak, A. Electron collision cross sections at low energies for all transitions between the n=1, 2, 3, 4 and 5 levels of atomic hydrogen. *J. Phys. B At. Mol. Phys.* **1991**, *24*, 1385–1410. [CrossRef]
200. Chen, G.X.; Pradhan, A.K. Atomic data from the Iron Project. XXXVII. Electron impact excitation collision strengths and rate coefficients for Fe VI. *Astron. Astrophys. Suppl. Ser.* **1999**, *136*, 395–403. [CrossRef]
201. Eissner, W.; Galavís, M.E.; Mendoza, C.; Zeippen, C.J. Atomic data from the IRON Project. XXXIV. Electron impact excitation of Fe XVI. *Astron. Astrophys. Suppl. Ser.* **1999**, *136*, 385–394. [CrossRef]
202. Eissner, W.; Galavís, M.E.; Mendoza, C.; Zeippen, C.J. Atomic data from the IRON Project. XXXVIII. Electron impact excitation of the fine-structure transitions in the n = 3 complex of Fe XV. *Astron. Astrophys. Suppl. Ser.* **1999**, *137*, 165–173. [CrossRef]
203. Garstang, R.H. Transition probabilities for forbidden lines of Fe II. *Mon. Not. R. Astron. Soc.* **1962**, *124*, 321, [CrossRef]
204. Nussbaumer, H.; Storey, P.J. Transition probabilities for Fe II infrared lines. *Astron. Astrophys.* **1988**, *193*, 327–333.
205. Giridhar, S.; Arellano Ferro, A. A Critical Compilation of Oscillator Strengths for Fe II Lines. *Rev. Mex. Astron. Astrofis.* **1995**, *31*, 23–37.
206. Nahar, S.N. Atomic data from the Iron Project. VII. Radiative dipole transition probabilities for Fe II. *Astron. Astrophys.* **1995**, *293*, 967–977.
207. Pelan, J.; Berrington, K.A. Atomic data from the IRON Project. IX. Electron excitation of the $^2P^\circ_{3/2}$–$^2P^\circ_{1/2}$ fine-structure transition in chlorine-like ions, from AR II to NI XII. *Astron. Astrophys. Suppl. Ser.* **1995**, *110*, 209.
208. Berrington, K.A.; Tully, J.A. Atomic data from the IRON Project. XXIV. Electron excitation of Li-like Fe XXIV between the N = 2 and n′ = 2, 3, 4 fine-structure levels. *Astron. Astrophys. Suppl. Ser.* **1997**, *126*, 105–111. [CrossRef]
209. Garstang, R.H. Energy levels and transition probabilities of Fe IV. *Mon. Not. R. Astron. Soc.* **1958**, *118*, 572. [CrossRef]
210. Kono, A.; Hattori, S. Accurate oscillator strengths for neutral helium. *Phys. Rev. A* **1984**, *29*, 2981–2988. [CrossRef]
211. Goett, S.J.; Sampson, D.H.; Clark, R.E.H. Intermediate-Coupling Collision Strengths for Transitions between Doubly Excited Levels Produced by Electron Impact on Highly Charged He-like Ions. *At. Data Nucl. Data Tables* **1983**, *28*, 279. [CrossRef]
212. Kaufman, V.; Sugar, J. Forbidden Lines in ns^2np^k Ground Configurations and nsnp Excited Configurations of Beryllium through Molybdenum Atoms and Ions. *J. Phys. Chem. Ref. Data* **1986**, *15*, 321–426. [CrossRef]
213. Nussbaumer, H.; Rusca, C. Forbidden transitions in the C I sequence. *Astron. Astrophys.* **1979**, *72*, 129–133. [CrossRef]
214. Mendoza, C. Recent advances in atomic calculations and experiments of interest in the study of planetary nebulae. In *Planetary Nebulae*; Flower, D.R., Ed.; D. Reidel Publishing Co.: Dordrecht, Holland, 1983; IAU Symposium 103; pp. 143–172.
215. Zeippen, C.J. Transition probabilities for forbidden lines in the $2p^3$ configuration. *Mon. Not. R. Astron. Soc.* **1982**, *198*, 111–125. [CrossRef]
216. Nahar, S.N.; Pradhan, A.K. Atomic data from the Iron Project. XVII. Radiative transition probabilities for dipole allowed and forbidden transitions in Fe III. *Astron. Astrophys. Suppl. Ser.* **1996**, *119*, 509–522. [CrossRef]
217. Butler, K.; Zeippen, C.J. N I forbidden lines revisited. *Astron. Astrophys.* **1984**, *141*, 274–278.
218. Bautista, M.A. Atomic data from the Iron Project. XXXIX. Photoionization cross sections and oscillator strengths for NI II. *Astron. Astrophys. Suppl. Ser.* **1999**, *137*, 529–535. [CrossRef]

219. Bautista, M.A. Continuum Fluorescence Excitation of [N I] and [O I] Lines in Gaseous Nebulae. *Astrophys. J.* **1999**, *527*, 474–478. [CrossRef]
220. Moore, C.E. *Selected Tables of Atomic Spectra. Atomic Energy Levels and Multiplet Table O III*; US Government Printing Office: Washington, DC, USA, 1985.
221. Thomas, L.D.; Nesbet, R.K. Low-energy electron scattering by atomic carbon. *Phys. Rev. A* **1975**, *12*, 2378–2382. [CrossRef]
222. Pequignot, D.; Aldrovandi, S.M.V. Effective collision strengths for the forbidden emission lines of neutral carbon, nitrogen and oxygen. *Astron. Astrophys.* **1976**, *50*, 141–144.
223. Johnson, C.T.; Burke, P.G.; Kingston, A.E. Electron scattering from the fine structure levels within the $1s^2 2s^2 2p^2\ ^3P^e$ ground state of C I. *J. Phys. B At. Mol. Phys.* **1987**, *20*, 2553–2563. [CrossRef]
224. Dopita, M.A.; Mason, D.J.; Robb, W.D. Atomic nitrogen as a probe of physical conditions in the interstellar medium. *Astrophys. J.* **1976**, *207*, 102–109. [CrossRef]
225. Berrington, K.A.; Burke, P.G. Effective collision strengths for forbidden transitions in e-N and e-O scattering. *Planet. Space Sci.* **1981**, *29*, 377–381. [CrossRef]
226. LeDourneuf, M.; Nesbet, R.K. Electron impact excitation of fine-structure levels of atomic oxygen. *J. Phys. B At. Mol. Phys.* **1976**, *9*, L241–L243. [CrossRef]
227. Zeippen, C.J.; Butler, K.; Le Bourlot, J. Effective collision strengths for fine-structure forbidden transitions in the $3p^3$ configuration of AR IV. *Astron. Astrophys.* **1987**, *188*, 251–257.
228. Krueger, T.K.; Czyzak, S.J. Excitation of Forbidden Lines in Gaseous Nebulae. II. Calculations for $3p^q$ Ions. *Proc. R. Soc. Lon. Ser. A* **1970**, *318*, 531–539. [CrossRef]
229. Mendoza, C.; Zeippen, C.J. Transition probabilities for forbidden lines in the $3p^2$ configuration-II. *Mon. Not. R. Astron. Soc.* **1982**, *199*, 1025–1032. [CrossRef]
230. Hayes, M.A. The S III intercombination multiplet—Radiative and electron excitation data. *J. Phys. B At. Mol. Phys.* **1986**, *19*, 1853–1862. [CrossRef]
231. Mendoza, C.; Zeippen, C.J. Transition probabilities for forbidden lines in the $3p^3$ configuration. *Mon. Not. R. Astron. Soc.* **1982**, *198*, 127–139. [CrossRef]
232. Fuhr, J.R.; Wiese, W.L. *RCR Handbook of Chemistry and Physics*, 71st ed.; CRC Press: Boca Raton, FL, USA, 1990.
233. Ramsbottom, C.A.; Bell, K.L.; Stafford, R.P. Effective Collision Strengths for Electron Impact Excitation of Singly Ionized Sulfur. *At. Data Nucl. Data Tables* **1996**, *63*, 57. [CrossRef]
234. Cai, W.; Pradhan, A.K. Excitation Rate Coefficients and Line Ratios for the Optical and Ultraviolet Transitions in S II. *Astrophys. J. Suppl. Ser.* **1993**, *88*, 329. [CrossRef]
235. Storey, P.J.; Mason, H.E.; Young, P.R. Atomic data from the IRON Project. XL. Electron impact excitation of the Fe XIV EUV transitions. *Astron. Astrophys. Suppl. Ser.* **2000**, *141*, 285–296. [CrossRef]
236. Saraph, H.E.; Storey, P.J. Atomic data from the IRON Project. XI. The $^2P^\circ_{1/2}$–$^2P^\circ_{3/2}$ fine-structure lines of AR VI, K VII and CA VIII. *Astron. Astrophys. Suppl. Ser.* **1996**, *115*, 151.
237. Zhang, H. Atomic data from the Iron Project. XVIII. Electron impact excitation collision strengths and rate coefficients for Fe III. *Astron. Astrophys.* **1996**, *119*, 523–528. [CrossRef]
238. Zhang, H.L.; Pradhan, A.K. Atomic data from the Iron Project. XXVII. Electron impact excitation collision strengths and rate coefficients for Fe IV. *Astron. Astrophys. Suppl. Ser.* **1997**, *126*, 373–378. [CrossRef]
239. Fernley, J.A.; Seaton, M.J.; Taylor, K.T. Atomic data for opacity calculations. VII. Energy levels, f values and photoionisation cross sections for He-like ions. *J. Phys. B At. Mol. Phys.* **1987**, *20*, 6457–6476. [CrossRef]
240. Peach, G.; Saraph, H.E.; Seaton, M.J. Atomic data for opacity calculations. IX. The lithium isoelectronic sequence. *J. Phys. B At. Mol. Phys.* **1988**, *21*, 3669–3683. [CrossRef]
241. Tully, J.A.; Seaton, M.J.; Berrington, K.A. Atomic data for opacity calculations. XIV. The beryllium sequence. *J. Phys. B At. Mol. Phys.* **1990**, *23*, 3811–3837. [CrossRef]
242. Fernley, J.A.; Hibbert, A.; Kingston, A.E.; Seaton, M.J. Atomic data for opacity calculations: XXIV. The boron-like sequence. *J. Phys. B At. Mol. Phys.* **1999**, *32*, 5507–5522. [CrossRef]
243. Luo, D.; Pradhan, A.K. Atomic data for opacity calculations. XI. The carbon isoelectronic sequence. *J. Phys. B At. Mol. Phys.* **1989**, *22*, 3377–3395. [CrossRef]
244. Hibbert, A.; Scott, M.P. Atomic data for opacity calculations. XXI. The neon sequence. *J. Phys. B At. Mol. Phys.* **1994**, *27*, 1315–1323. [CrossRef]
245. Butler, K.; Mendoza, C.; Zeippen, C.J. Atomic data for opacity calculations. XIX. The magnesium isoelectronic sequence. *J. Phys. B At. Mol. Phys.* **1993**, *26*, 4409–4423. [CrossRef]
246. Mendoza, C.; Eissner, W.; LeDourneuf, M.; Zeippen, C.J. Atomic data for opacity calculations. XXIII. The aluminium isoelectronic sequence. *J. Phys. B At. Mol. Phys.* **1995**, *28*, 3485–3504. [CrossRef]
247. Nahar, S.N.; Pradhan, A.K. Atomic data for opacity calculations. XVIII. Photoionization and oscillator strengths of Si-like ions Si^0, S^{2+}, Ar^{4+}, Ca^{6+}. *J. Phys. B At. Mol. Phys.* **1993**, *26*, 1109–1127. [CrossRef]
248. Bautista, M.A. Atomic data from the Iron Project. XVI. Photoionization cross sections and oscillator strengths for Fe V. *Astron. Astrophys. Suppl. Ser.* **1996**, *119*, 105–110. [CrossRef]

249. Bautista, M.A.; Pradhan, A.K. Atomic data from the Iron Project. XXVI. Photoionization cross sections and oscillator strengths for Fe IV. *Astron. Astrophys. Suppl. Ser.* **1997**, *126*, 365–371. [CrossRef]
250. Nahar, S.N. Photoionization cross sections and oscillator strengths for Fe III. *Phys. Rev. A* **1996**, *53*, 1545–1552. [CrossRef]
251. Nahar, S.N.; Pradhan, A.K. Atomic data for opacity calculations: XX. Photoionization cross sections and oscillator strengths for Fe II. *J. Phys. B At. Mol. Phys.* **1994**, *27*, 429–446. [CrossRef]
252. Bautista, M.A. Atomic data from the IRON Project. XX. Photoionization cross sections and oscillator strengths for Fe I. *Astron. Astrophys. Suppl. Ser.* **1997**, *122*, 167–176. [CrossRef]
253. Gorczyca, T.W. Auger decay of the photoexcited $1s^{-1}np$ Rydberg series in neon. *Phys. Rev. A* **2000**, *61*, 024702. [CrossRef]